crystals

MDPI

Article

Correlation between Structural and Transport Properties of Ca-Doped La Nickelates and Their Electrochemical Performance

Elena Pikalova [1,2,*], Vladislav Sadykov [3,4], Ekaterina Sadovskaya [3], Nikita Yeremeev [3], Alexander Kolchugin [1], Alexander Shmakov [3,5,6], Zakhar Vinokurov [3,5,6], Denis Mishchenko [3,4], Elena Filonova [7] and Vladimir Belyaev [3]

1 Institute of High Temperature Electrochemistry UB RAS, 620066 Yekaterinburg, Russia; laba50@mail.ru
2 Department of Environmental Economics, Graduate School of Economics and Management, Ural Federal University Named after the First President of Russia B.N. Yeltsin, 620002 Ekaterinburg, Russia
3 Federal Research Center Boreskov Institute of Catalysis, 630090 Novosibirsk, Russia; sadykov@catalysis.ru (V.S.); sadovsk@catalysis.ru (E.S.); yeremeev21@gmail.com (N.Y.); shurka@catalysis.ru (A.S.); vinzux@mail.ru (Z.V.); q14999@yandex.ru (D.M.); belyaev@catalysis.ru (V.B.)
4 Department of Natural Sciences, Novosibirsk State University, 630090 Novosibirsk, Russia
5 Budker Institute of Nuclear Physics SB RAS, 630090 Novosibirsk, Russia
6 Department of Physics, Novosibirsk State University, 630090 Novosibirsk, Russia
7 Department of Physical and Inorganic Chemistry, Institute of Natural Sciences and Mathematics, Ural Federal University Named after the First President of Russia B.N. Yeltsin, 620002 Ekaterinburg, Russia; elena.filonova@urfu.ru
* Correspondence: e.pikalova@list.ru

Abstract: This work presents the results from a study of the structure and transport properties of Ca-doped $La_2NiO_{4+\delta}$. $La_{2-x}Ca_xNiO_{4+\delta}$ (x = 0–0.4) materials that were synthesized via combustion of organic-nitrate precursors and characterized by X-ray diffraction (XRD), in situ XRD using synchrotron radiation, thermogravimetric analysis (TGA) and isotope exchange of oxygen with $C^{18}O_2$. The structure was defined as orthorhombic (*Fmmm*) for x = 0 and tetragonal (*I4/mmm*) for x = 0.1–0.4. Changes that occurred in the unit cell parameters and volume as the temperature changed during heating were shown to be caused by the excess oxygen loss. Typical for Ruddlesden–Popper phases, oxygen mobility and surface reactivity decreased as the Ca content was increased due to a reduction in the over-stoichiometric oxygen content with the exception of x = 0.1. This composition demonstrated its superior oxygen transport properties compared to $La_2NiO_{4+\delta}$ due to the enhanced oxygen mobility caused by structural features. Electrochemical data obtained showed relatively low polarization resistance for the electrodes with a low Ca content, which correlates well with oxygen transport properties.

Keywords: $La_2NiO_{4+\delta}$; Ca doping; isotope exchange; synchrotron radiation studies; oxygen mobility; polarization resistance

check for updates

Citation: Pikalova, E.; Sadykov, V.; Sadovskaya, E.; Yeremeev, N.; Kolchugin, A.; Shmakov, A.; Vinokurov, Z.; Mishchenko, D.; Filonova, E.; Belyaev, V. Correlation between Structural and Transport Properties of Ca-Doped La Nickelates and Their Electrochemical Performance. *Crystals* **2021**, *11*, 297. https://doi.org/10.3390/cryst11030297

Academic Editor: Christian Rodenbücher

Received: 27 February 2021
Accepted: 15 March 2021
Published: 17 March 2021

1. Introduction

Oxides with a perovskite-related Ruddlesden–Popper (R–P) structure, particularly $Ln_2NiO_{4+\delta}$ (Pr, Nd, La), have been reported to have high levels of mixed ionic and electronic conductivity in addition to fast oxygen transport [1–5]. Such properties are among the main requirements for oxygen separation membranes and air electrodes of intermediate temperature electrochemical devices [6–11]. The layered structure of $Ln_2NiO_{4+\delta}$ consists of $LnNiO_3$ perovskite-type layers alternating with Ln_2O_2 rock salt layers. The characteristic feature of $Ln_2NiO_{4+\delta}$ is its ability to accommodate interstitial oxygen anions, preferably within the rock salt layers, resulting in an oxygen excess. According to the literature data, at ambient temperatures, in $La_2NiO_{4+\delta}$, the δ value can reach 0.13–0.18 [12–14], and for $Pr_2NiO_{4+\delta}$ and $Nd_2NiO_{4+\delta}$, the oxygen excess can be as high as 0.25–0.27 [15–17]. At higher temperatures and with low oxygen partial pressure, the concentration of interstitial atoms

decreases remarkably [18,19]. High values of the oxygen tracer [8,20,21] and chemical diffusion coefficients [22] for Ln nickelates (~10^{-8}–10^{-5} cm s^{-1} at 700 °C) are associated with the migration of oxygen through a cooperative mechanism, involving both regular and highly mobile interstitial oxygen positions [8,23,24].

Oxides such as $Ln_2NiO_{4+\delta}$ can be doped both in the Ln or Ni positions to give a wide range of materials with advanced functional properties [6,9,25,26]. For instance, substitution in the Ln position with alkaline earth elements significantly increases the level of electronic conductivity of nickelates. This is a necessary requirement for both the effective operation of the electrodes and for the application of these materials as mixed ionic and electronic conductor (MIEC) membranes because it elevates the ambipolar conductivity level—the crucial characteristic of the membranes. It has been reported for $La_{2-x}Sr_xNiO_{4+\delta}$ that when the strontium content is increased, the electrical conductivity significantly increases from 50 S cm^{-1} (at 1000 °C) for the undoped $La_2NiO_{4+\delta}$ and up to 200–250 S cm^{-1} (at 1000 °C) for Sr-rich samples (x = 0.75, 1) [14,27]. For $La_{2-x}Ca_xNiO_{4+\delta}$, an increase in calcium content similarly elevates the total conductivity from 80–95 S cm^{-1} for the undoped $La_2NiO_{4+\delta}$ and up to 90–165 S cm^{-1} (at 400 °C) for Ca-rich samples ($x \geq 0.2$) [9,22,28,29]. Due to the lower substitution level for Ca in the $La_2NiO_{4+\delta}$ compared with Sr, the attainable enhancement in conductivity is also lower. However, at the same x values, Ca-doped systems demonstrate higher conductivity values compared to those for Sr- or Ba-doped systems [30].

It was shown for $La_{2-x}Ca_xNiO_{4+\delta}$ that its ionic conductivity had no direct correlation with Ca content, attaining the maximum at x = 0.1 (3–10 mS cm^{-1} in the range of 600–700 °C [29]. The authors reported that the activation energy for oxygen ion conductivity decreased when increasing the calcium doping level. This is due to elongation of the La–O2 bond length, which corresponds to the thickness of the La_2O_2 layer, providing a larger space for oxygen migration and thus enhancing the mobility of oxygen ions. However, doping with Ca, as well as with other alkaline earth elements, results in the interstitial oxygen content being reduced [21]. It is these two opposite trends that give the maximum ionic conductivity for $La_{1.9}Ca_{0.1}NiO_{4+\delta}$. Similarly, the oxygen mobility in the $La_{2-x}Ca_xNiO_{4+\delta}$ (x = 0–0.2) series under a chemical potential gradient was reported to have a non-linear x dependence according to the electrical conductivity relaxation data, with the best properties for x = 0.1 [22]. According to isotope exchange of oxygen and ionic conductivity measurement data, a decrease in the oxygen tracer diffusion coefficient with Ca content was demonstrated to be associated with a reduction in highly mobile interstitial oxygen content as a charge-compensating mechanism while substituting La^{3+} with Ca^{2+} [19,28,29,31,32]. However, whether such a dependence is consistent or not still remains unclear. According to [32], there was a consistent decrease both in oxygen tracer diffusion coefficient and oxide ionic conductivity values when increasing the Ca content for $La_{2-x}Ca_xNiO_{4+\delta}$ (x = 0–0.3). However, in [29] it was reported that oxygen tracer diffusion coefficient concentration dependence had non-linear behavior, with a maximum for $La_{1.9}Ca_{0.1}NiO_{4+\delta}$.

In the present paper, the structural and transport properties of $La_{2-x}Ca_xNiO_{4+\delta}$ (x = 0–0.4) are investigated using various methods including in situ powder X-ray diffraction (XRD), temperature-programmed isotope exchange (TPIE) of oxygen, electrical impedance spectroscopy and thermogravimetric analysis (TGA) to elucidate how Ca content affects the overall performance of the $La_{2-x}Ca_xNiO_{4+\delta}$ oxides and electrochemical characteristics of the related electrodes.

2. Materials and Methods

2.1. Synthesis

Materials of the $La_{2-x}Ca_xNiO_{4+\delta}$ (x = 0–0.4) series were prepared via combustion of organic-nitrate precursors. $Ni(NO_3)_2{\cdot}4H_2O$ (>99% of purity), $Ca(NO_3)_2{\cdot}4H_2O$ (99%) and $La(NO_3)_3{\cdot}6H_2O$ (99%) were selected as raw materials for the synthesis. The initial reagents and organic fuels such as glycine and glycerol, taken in a ratio of 1.5:0.5:1 to the

metals, were dissolved and mixed in distilled water. Excess water was evaporated from the mixture by continuous heating at 100 °C; in a drying oven until a gel state was attained. A 10% NH_4OH solution was added to set the pH value in the gel precursor equal to 8–9, and then it was further heated up to 300 °C to initiate a self-ignition process. The resulting black cake was then ground into a powder and calcinated at 500 °C (5 h) and 1000 °C (5 h) with intermediate grinding in a Pulverisette 6 planetary mill (Fritsch, Germany) (plastic drums, stainless steel milling bodies). The final calcination of materials was performed at 1150 °C for 5 h. The obtained materials were ball-milled to obtain electrode powders. The powder's specific surface area, measured by a Brunauer–Emmett–Teller (BET) method using a META SORBI N 4.1 instrument, was in the range of 1.24–1.63 $m^2\ g^{-1}$. The BET data are presented in Table S1 (Supplementary Materials). The samples were designated as LNO ($La_2NiO_{4+\delta}$) and LCNO01–LCNO04 ($La_{2-x}Ca_xNiO_{4+\delta}$), respectively.

2.2. Structural Characterization

The X-ray diffraction (XRD) analysis of the powdered materials taken after the final synthesis step was performed using an XRD-7000 diffractometer (Shimadzu, Kyoto, Japan) configurated with a graphite monochromator with CuK_α radiation (angle range of $23^\circ \leq 2\theta \leq 81^\circ$, scan step of 0.02°, exposure time of 5 s). The refinement of the crystal structure in the $La_{2-x}Ca_xNiO_{4+\delta}$ series was performed on the basis of the XRD data obtained by the Rietveld method using a FullProf Suite software package [33]. To elucidate some structural peculiarities of as-prepared samples as well as the samples after in situ X-ray diffraction experiments, additional XRD patterns were collected using an anomalous scattering station located at the Siberian Synchrotron and Terahertz Radiation Centre (Budker Institute of Nuclear Physics SB RAS, Novosibirsk [34]). The radiation wavelength of 0.15402 nm during measurements was set by a Si (111) double-crystal monochromator.

In situ X-ray diffraction experiments were carried out at a precision diffractometry-2 station located at the Siberian Synchrotron and Terahertz Radiation Centre (Budker Institute of Nuclear Physics SB RAS, Novosibirsk [34]). The station is equipped with an OD-3M single-coordinate, position-sensitive detector (Institute of Nuclear Physics SB RAS [35]), an XRK 900 high-temperature X-ray chamber-reactor (Anton Paar, Graz, Austria) and a gas mixture feed system controlled by SEC-Z500 digital mass flow meters (Horiba Ltd., Kyoto, Japan). The radiation wavelength of 0.101 nm during measurements was set by single reflection of the incoming white synchrotron radiation (SR) beam from a Si (220) single crystal. The oxygen partial pressure during measurements was monitored using a UGA-100 quadrupole-type gas analyzer (Stanford Research System Inc., Sunnyvale, CA, USA) connected to the reactor outlet through a PEEK capillary. High temperature in situ XRD measurements in a $He+O_2$ gas mixture (pO_2 = 0.2 atm) were carried out on the powdered $La_{2-x}Ca_xNiO_{4+\delta}$ (x = 0–0.4) samples initially pretreated in He (700 °C). The data were collected upon the samples being heated from 30 to 700 °C and cooling down to 30 °C at a rate of 10 °C min^{-1}.

2.3. Oxygen Over-Stoichiometry Studies

Thermogravimetric analysis (TGA) and differential scanning calorimetry (DSC) studies were conducted using a NETZSCH STA 409 PC Luxx machine (Netzsch, Germany). The following cycles were carried out:

(1) pretreatment in synthetic air (21 vol.% of oxygen in Ar), flow rate of 50 mL min^{-1}, from 30 to 1000 °C and back, heating/cooling ramp of 10 °C min^{-1};
(2) treatment in synthetic air, flow rate of 50 mL min^{-1}, from 30 to 1000 °C and back, heating/cooling ramp of 10 °C min^{-1};
(3) treatment in H_2-containing atmosphere (10 vol.% of H_2 in Ar), flow rate of 50 mL min^{-1}, from 30 to 1000 °C and back, heating/cooling ramp of 10 °C min^{-1}.

The absolute oxygen content in the materials of the $La_{2-x}Ca_xNiO_{4+\delta}$ series was calculated based on the following reduction reaction:

$$La_{2-x}Ca_xNiO_{4+\delta} + gH_2 \rightarrow 0.5(2-x)La_2O_3 + xCaO + Ni + gH_2O \quad (1)$$

where $g = 1 + 0.5x + \delta$. As an example, temperature dependences of mass loss and DSC curves for the LNO and LCNO01 samples collected upon reduction in the H_2-containing atmosphere are shown in Figure S1 (Supplementary Materials).

2.4. Oxygen Mobility and Surface Reactivity Studies

In order to study oxygen transport properties, experiments regarding oxygen isotope exchange in temperature-programmed mode (TPIE) were carried out in a flow reactor. Ground samples (fraction 0.25–0.5 mm, weight 50 mg) were loaded into a tubular quartz reactor with an inner diameter of 3 mm. Pretreatment was carried out at 700 °C for 30 min in a flow of He + 1% O_2 (flowrate of 25 mL min^{-1}). Treatment was conducted in the temperature range of 50–800 °C with a temperature ramp of 5 °C min^{-1} in a flow of He + 1% $C^{18}O_2$ + 1% Ar (flow rate of 25 mL min^{-1}). The transient changes in the gas isotopic composition ($C^{16}O_2$, $C^{16}O^{18}O$ and $C^{18}O_2$ concentrations) at the reactor outlet were monitored by an SRS 200 (Stanford Research Systems, USA) mass spectrometer using UGA software. An atomic fraction of ^{18}O (α) in CO_2 was calculated based on the following mass-spectrometric data: $\alpha = (0.5 \times I_{46} + I_{48})/(I_{44} + I_{46} + I_{48})$, where I_{44}, I_{46} and I_{48} were parent peaks at m/e 44, 46, 48.

The analysis of the temperature dependences of α was carried out by a mathematical model including the exchange of oxygen in the oxide surface ($O_{(surf)}$) with CO_2 molecules in the gas phase with a rate R (heteroexchange rate), oxygen diffusion within the oxide bulk via fast channel with a coefficient D^* and exchange between the most mobile oxide anions and neighboring strongly bound oxide anions with a weighted average rate of β [36]. The oxygen surface exchange constant was calculated as follows: $k^* = R/(\rho N_O)$, where ρ and N_O were sample true density and amount of oxygen per unit mass, respectively. The error of calculating R, D^*, β and their effective activation energies did not exceed ±15%.

2.5. Electrochemical Characterization of the $La_{2-x}Ca_xNiO_{4+\delta}$ Electrodes

Electrochemical characterization of electrodes based on the materials of the $La_{2-x}Ca_xNiO_{4+\delta}$ series was performed by an electrochemical impedance spectroscopy (EIS) method on $Ce_{0.8}Sm_{0.2}O_{1.9}$ (SDC) electrolyte substrates. For the substrates' fabrication, SDC material was synthesized via a solid-state reaction method from CeO_2 (CeO-L grade, of 99.99% purity) and Sm_2O_3 (SmO-L grade, of 99.99% purity). The starting reagents were mixed in the planetary mill, dried and calcined at 1050 °C, 2 h. Next, the obtained powder was ball milled and dry pressed into disks at 150 MPa with following sintering at 1550 °C, 3 h. According to the XRD analysis performed on the SDC powder obtained by grinding the sintered disk-shape samples, it was single phase with a fluorite type structure ($Fm\bar{3}m$ *sp. gr.*) and a unit cell parameter of a = 5.5453 (6) Å, which correlated well with the value presented in the literature [37]. The relative density of the substrates calculated from their geometrical sizes and weight was 95%. Additionally, a $LaNi_{0.6}Fe_{0.4}O_3$ (LNF) powder for the formation of the electrode collectors was synthesized by a Pechini method; details of the synthesis procedure are given elsewhere [28,30]. The LNF powder possessed a rhombohedral structure ($R\bar{3}c$ *sp. gr.*) with unit cell parameters of a = 5.5036 (2) Å and c = 13.2602 (5) Å.

The $La_{2-x}Ca_xNiO_{4+\delta}$ slurries for the electrode formation were prepared by mixing the ball-milled powders with ethyl alcohol and a polyvinyl butyral binder. The electrode layers were painted symmetrically on the SDC electrolyte substrates with an effective area of 0.25–0.36 cm^2 and a deposition density of 8–10 mg/cm^2. The thickness of the electrode layers evaluated after the sintering at 1250 °C for 1 h was 25 ± 3 μm. The LNF collector of the same thickness was deposited onto the pre-sintered LCNO electrode layers and sintered

at 1200 °C for 1 h. The morphology of the electrodes was characterized by a JSM-5900LV (JEOL USA, Inc., Peabody, MA, USA) scanning electron microscope.

The electrochemical study was carried out by means of a SL-1260 impedance/gain-phase analyzer and a SL-1287 potentiostat/galvanostat electrochemical interface (Solartron Analytical, Farnborough, UK). The spectra collected in air in the temperature range of 550–850 °C were fitted using ZView 2 software.

3. Results and Discussion

3.1. Structural Features of the $La_{2-x}Ca_xNiO_{4+\delta}$ Materials in Air at Room Temperature

On the basis of the XRD data, profile and structural parameters for the $La_{2-x}Ca_xNiO_{4+\delta}$ materials (denoted as LNO at x = 0.0 and LCNO01-LCNO04 at x = 0.1–0.4, see Table S1, Supplementary Materials) were refined by a full-profile Rietveld refinement method. Experimental and calculated profiles of the LNO and LCNO01-LCNO04 powders' XRD patterns acquired using a model of La and Ca cations' uniform distribution are given in Figures S2–S6 (Supplementary Materials). The structure refinement results are provided in Table 1.

Table 1. Profile features, structural parameters and interatomic distances for $La_{2-x}Ca_xNiO_{4+\delta}$ samples according to the X-ray diffraction (XRD) and thermogravimetric analysis (TGA) data.

x		x = 0.0	x = 0.1	x = 0.2	x = 0.3	x = 0.4
t, *including* δ		0.898	0.897	0.899	0.899	0.898
structure		O	T	T	T	T
a, [Å]		5.4628(4)	3.8557(1)	3.8429(1)	3.8303(1)	3.8173(1)
b, [Å]		5.4664(4)	3.8557(1)	3.8429(1)	3.8303(1)	3.8173(1)
c, [Å]		12.6827(4)	12.6596(3)	12.6277(3)	12.6032(2)	12.5831(3)
V, [Å^3]		378.74(4)	188.21(1)	186.49(1)	184.90(1)	183.36(1)
ρ, [g cm^{-3}]		7.02	6.89	6.78	6.66	6.54
z(La/Ca)		0.3605(1)	0.3608(1)	0.3613(1)	0.3618(1)	0.3618(1)
z(O2)		0.173(1)	0.173(1)	0.175(1)	0.176(1)	0.176(1)
Bov		0.52(4)	0.59(3)	0.42(4)	0.49(4)	0.64(3)
L, [Å]	La/Ca-La/Ca	3.538(1)	3.525(1)	3.504(2)	3.483(1)	3.477(1)
	Ni-La/Ca	3.254(1)	3.247(1)	3.233(1)	3.220(1)	3.211(1)
	Ni-Ni	3.8641(1)	3.8557(1)	3.8429(1)	3.8303(1)	3.8173(1)
	Ni-O1x4	1.9320(1)	1.9279(1)	1.9215(1)	1.9151(1)	1.9086(1)
	Ni-O2x2	2.20(1)	2.19(1)	2.21(1)	2.21(1)	2.21(1)
	La/Ca-O1x4	2.620(1)	2.612(1)	2.600(1)	2.589(1)	2.582(1)
	La/Ca-O2x4	2.765(1)	2.759(1)	2.756(1)	2.749(1)	2.741(1)
	La/Ca-O2x1	2.38(1)	2.38(1)	2.35(1)	2.35(1)	2.34(1)
R_{exp}		4.40	4.52	4.25	4.31	4.24
R_p		7.94	7.15	9.12	7.90	7.74
R_{wp}		10.0	9.47	11.8	10.3	9.88
R_{Br}		3.75	3.21	3.13	2.86	3.34
R_f		2.21	2.15	2.14	2.31	2.30
χ^2		5.21	4.38	7.70	5.87	5.33
δ		0.17(1)	0.11(1)	0.09(1)	0.05(1)	0.00(1)
Tc, °C		300	340	280	270	n/a
$-\partial\delta/\partial T \times 10^5$, K^{-1}		12.7	11.8	10.1	4.1	1

According to the profile analysis data, the LNO sample was determined to have an orthorhombic crystal unit cell (*Fmmm sp. gr.*). This conclusion can be illustrated by the fragments of the XRD patterns obtained using the synchrotron data for the LNO and LCNO01 samples and taken in the range of high diffraction angles demonstrated in Figure 1. Orthorhombic splitting of the XRD peaks with Miller indices of (*2 0 10*), (*0 2 10*); (*4 0 6*), (*0 4 6*); (*4 2 4*), (*2 4 4*) was clearly observed for the LNO sample (Figure 1a), while the peaks with these indices were indistinguishable for the LCNO01 sample (Figure 1b), which was determined to possess a tetragonal crystal structure (*I4/mmm sp.gr.*). It is

known that embedding the interstitial oxygen in a K_2NiF_4-type structure weakens lattice micro-strains that appear as a consequence of mismatch between the perovskite and rock salt layers in the *ab* plane. To estimate the micro-strains' level in such perovskite-like structures, the Goldschmidt tolerance factor (*t*) is typically used [38]. Calculated *t* values for the LCNO series are given in Table 1. Doping with Ca is characterized by strain relief in the LNO structure, which, in turn, results in the structure stabilizing in a tetragonal syngony and the over-stoichiometric oxygen content decreasing. The *t* value changes in the series due to the following contributions: (1) the Ca ionic radius is lower compared to that of La (rCa^{2+}_{IX} = 1.18 Å, rLa^{3+}_{IX} = 1.216 Å [39]); (2) the radius of Ni^{3+} cations forming due to Ca doping is lower compared to that of Ni^{2+} ($rNi^{3+}_{VI} = 0.56_{LS}$ Å; 0.60_{HS} Å, rNi^{2+}_{VI} = 0.69 Å) [39]). The Ni^{3+} content is controlled both by the Ca content and the oxygen stoichiometry, which provide opposite contributions, respectively. Calculated using the experimental oxygen over-stoichiometry data, the tolerance factor values show no trends in the series (Table 1).

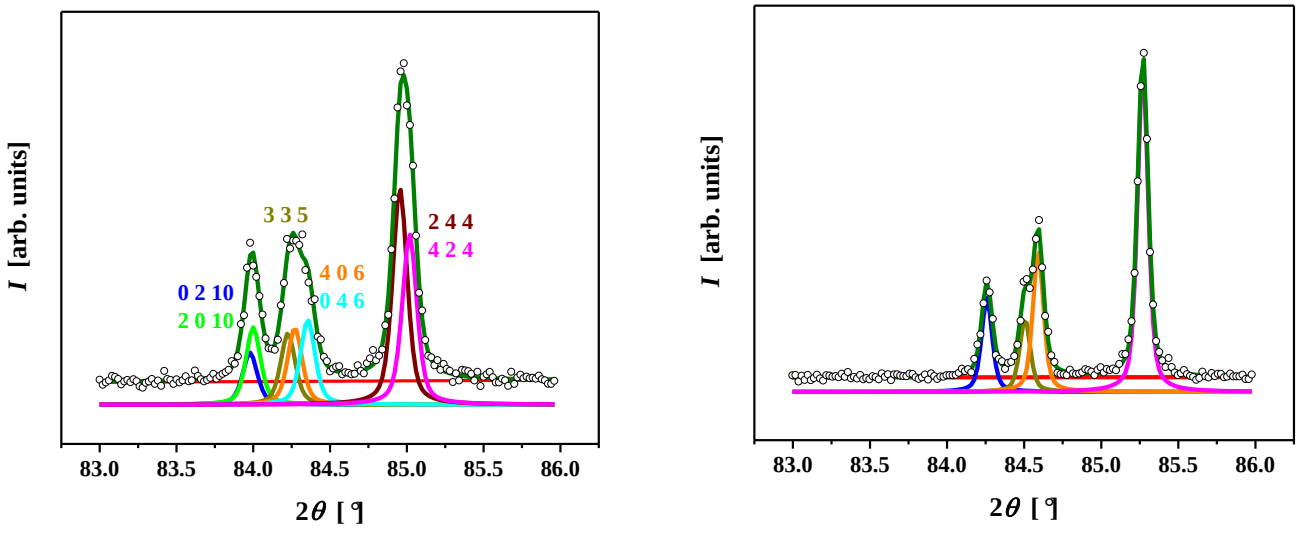

Figure 1. Experimental XRD patterns of the $La_2NiO_{4+\delta}$ (**a**) and $La_{1.9}Ca_{0.1}NiO_{4+\delta}$ (**b**) samples illustrating the phase transition from an orthorhombic to a tetragonal structure with Ca doping. XRD data were obtained at the Anomalous Scattering station (SSRTC, Novosibirsk) at a wavelength of 0.15402 nm.

Structural phase transitions from an orthorhombic to a tetragonal syngony while substituting lanthanide cations with alkaline earth metals in $Ln_{2-x}M_xNiO_{4+\delta}$, governed by a reduction in the over-stoichiometric oxygen content, had been observed earlier in a number of studies for $La_{2-x}Ca_xNiO_{4+\delta}$ [28], $La_{2-x}Sr_xNiO_{4+\delta}$ [27], $Nd_{2-x}Ca_xNiO_{4+\delta}$ [40] and $Pr_{2-x}Ca_xNiO_{4+\delta}$ [41]. Contrarily, the $La_{2-x}M_xNiO_{4+\delta}$ materials (where M is an alkaline earth metal) possessing a tetragonal structure across the entire range of the dopant content were obtained in [13,29,32,42–45]. The $Ln_2NiO_{4+\delta}$ crystal structure is known to depend on synthesis conditions determining the oxygen over-stoichiometry (δ) value [1]. Formation of the orthorhombic structure for the undoped LNO sample obtained in the current work by combustion of organic-nitrate precursors with a relatively low synthesis temperature reveals the presence of a high content of over-stoichiometric (interstitial) oxygen in its structure. This was determined, according to the TGA data shown in Figure S1, to be equal to 0.17, is higher compared to the δ value given in the works marked above (e.g., δ = 0.14 in [43,44]) and is in agreement with the phase diagram for LNO plotted in [20]. According to the conclusions of Tamura H. et al. [13], the LNO samples with an oxygen over-stoichiometry value in the range of $0.15 < \delta \leq 0.18$ possess an orthorhombic structure (*Fmmm sp. gr.*), while those whose range is $0.10 \leq \delta \leq 0.15$ have a tetragonal structure (*I4/mmm sp. gr.*), with the existence of a two-phase region between them. It is the

presence of a possible phase separation that can explain the formation of the orthorhombic (*Fmmm sp. gr.*) structure for LNO with δ = 0.11–0.15 in [20] and the formation of the tetragonal structure for LNO with δ = 0.16 [46].

Concentration dependences of the unit cell parameters and volume for the LCNO series are provided in Figure 2 (for the sake of comparison, the orthorhombic unit cell parameters for the LNO sample were refitted to tetragonal). The observed linear decrease in the unit cell parameters and volume along with an increase in the Ca content, governed by the size factors, concurs closely with Vegard's law and is evidence of the formation of a true solid-state solution. The shape of the dependences obtained for the LCNO series in the current work is in good agreement with the data provided in the studies [29,32,42–45].

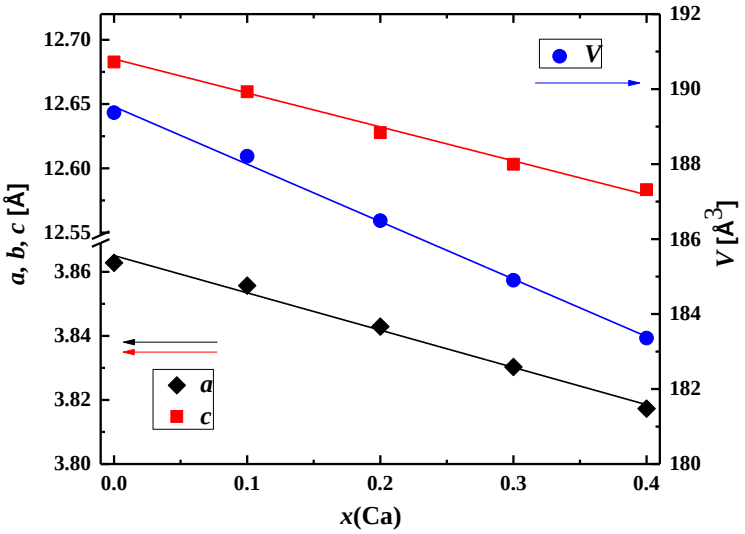

Figure 2. Ca content dependences of unit cell parameters and volume for the $La_{2-x}Ca_xNiO_{4+\delta}$ samples according to the Rietveld refinement of the XRD data.

The marked tendency for the unit cell parameters to decrease as the substitution level in the LCNO series increases can be illustrated by the data on the calculations of the bonds' lengths (Figure 3a,b). The unit cell parameter *a* in the tetragonal structure is determined by the Ni–O1 bond length, which decreases as the Ca content increases, as follows from Figure 3a. The unit cell parameter *c* is equal to the sum of the doubled Ni–O2 distance (Figure 3a), the La/Ca–La/Ca distance along the *c* axis (Figure 3a) and the doubled La/Ca–O2x1 distance (Figure 3b). As follows from Figure 3a, while increasing the Ca content, the La/Ca–La/Ca bond length decreases, the La/Ca–O2x1 decreases at $x \geq 0.2$ and the Ni–O2 bond length remains relatively constant. This results in the *c* parameter steadily and consistently decreasing (Figure 2).

Another parameter used to analyze the stability of the LCNO structure is a global instability index (GII) [42]. High GII values for heavily doped samples indicate instability of crystal structure (Table S2). The La/Ca–O2x1 bond length corresponds to the rock salt layer thickness, and when analyzing its concentration dependence, one can conclude that doping with calcium leads to a reduction in the rock salt layer thickness at $x \geq 0.2$, which will destabilize the LCNO structure at high *x* values as a result. This is supported by the high values of the global instability index (GII) for the LCNO series with high calcium content ($x > 0.3$) (Table S2), which agrees with [42] and explains the lower level of the Ca substitution limit for the La position in the LNO structure compared to that of Sr [43]. Taking into account both the variation of the tolerance factor and GII with increasing Ca content, it can be concluded that the Ca doping makes the structure more unstable in the series.

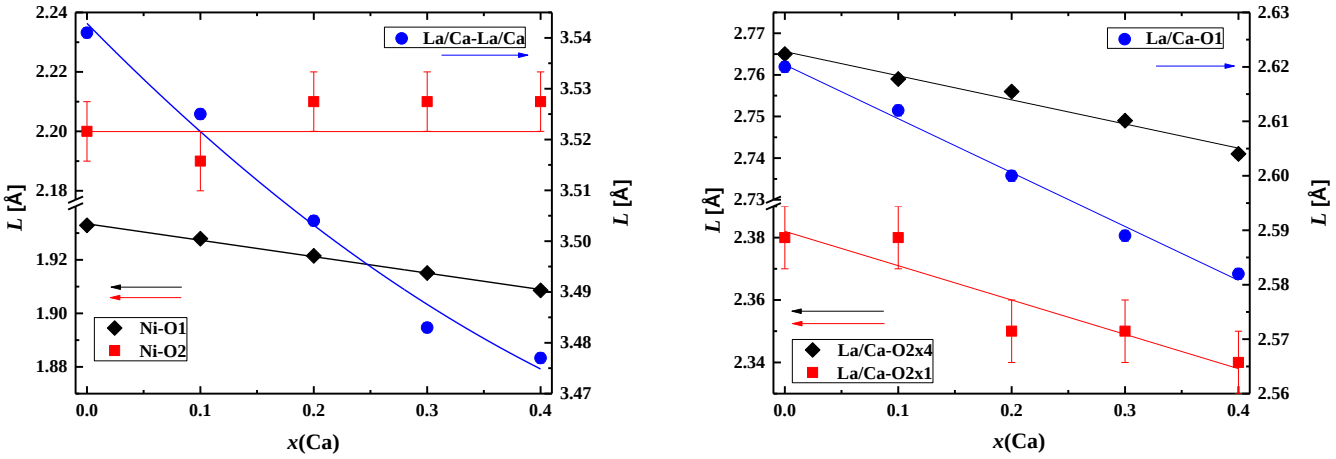

(**a**) (**b**)

Figure 3. Ca content dependences of the Ni-O and La/Ca-La/Ca bond lengths (**a**) and the La/Ca-O bond lengths in $La_{2-x}Ca_xNiO_{4+\delta}$ according to the Rietveld refinement of the XRD data (**b**).

3.2. Oxygen Over-Stoichiometry Studies

As follows from the TGA data, there was a sharp decrease in the δ values even at a low Ca doping level. For example, for the LCNO01 sample, the δ value was equal to 0.11 as compared to 0.17 for the LNO sample, while for the LNCO04 sample, it was as low as 0.00 (all values are presented in Table 1). This is due to La^{3+} substitution with Ca^{2+}, leading to a decrease in the interstitial oxygen content by a charge compensation mechanism [19,21,28,29,31,32]:

$$2La_{La}^{\times} + O_O^{\times} + 2CaO \rightleftarrows 2Ca'_{La} + V_O^{\bullet\bullet} + La_2O_3, \quad (2)$$

$$O_O^{\times} + V_i^{\times} \rightleftarrows O_i'' + V_O^{\bullet\bullet}, \quad (3)$$

where $O_O^{\times}$ is an oxygen ion in the regular lattice site, O_i'' is an interstitial oxygen ion in the rock salt layer, $V_i^{\times}$ is an interstitial vacancy, $V_O^{\bullet\bullet}$ is an oxygen vacancy in the perovskite-type layer. Thus, the observed tendency for the oxygen over-stoichiometry to decrease with Ca doping and the level of the δ-values for the Ca-doped samples obtained in this study are in good agreement with those stated in the literature.

The analysis of the temperature dependences of oxygen over-stoichiometry calculated from the TGA data obtained in air (Figure 4a) showed that with Ca doping, there was not only a decrease in δ values, but also a gradual reduction in the rate of oxygen release upon heating. This was calculated as $-\partial\delta/\partial T$ in the temperature range above T_c (T_c values are related to the end of a low-temperature "plateau" on the curves when the oxygen exchange of the samples with the ambient air starts) was observed (Table 1). This is in agreement with temperature-programmed desorption of oxygen and TGA data for $La_2NiO_{4+\delta}$ and other R–P phase samples, including the ones doped with alkaline earth metals [47–51]. The T_c values did not show direct concentration dependence and were in the range of 270–340 °C, with the highest T_c of 340 °C for LCNO01. The analysis of the concentration dependence of oxygen over-stoichiometry (inset in Figure 4a) shows that the LNCO01 sample exhibits unexpectedly more relaxed structure (lesser δ values than could be assumed from linear approximation). This may explain the higher T_c temperature observed for LCNO01.

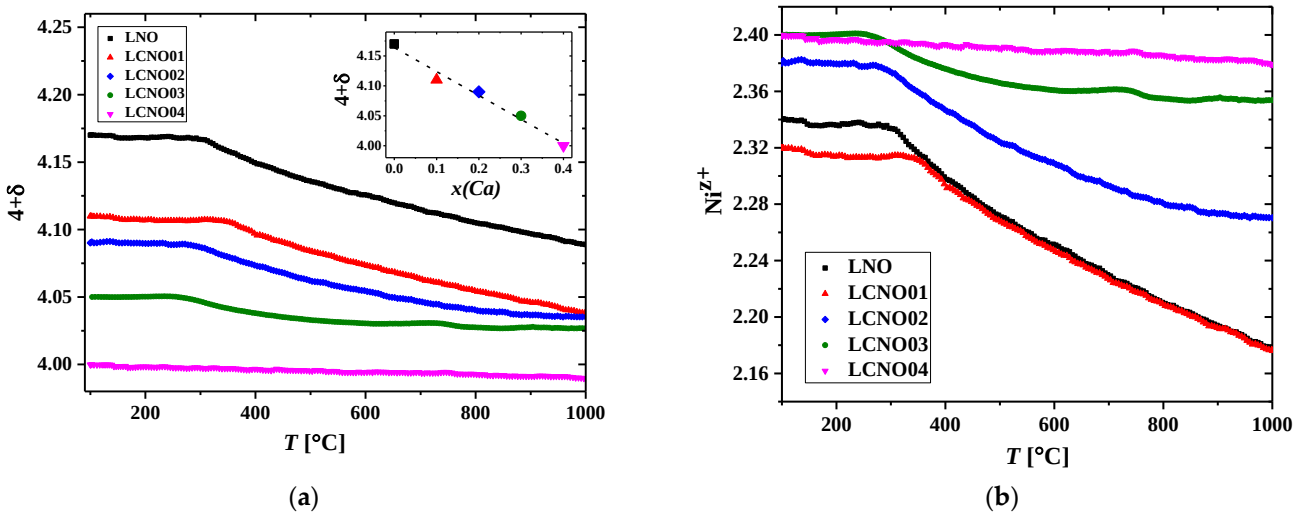

Figure 4. Temperature dependences of oxygen stoichiometry (**a**) and formal Ni oxidation state (**b**) for the $La_{2-x}Ca_xNiO_{4+\delta}$ series calculated from the TGA data collected upon heating in air.

Figure 4b shows the average formal Ni cation oxidation state calculated from the oxygen over-stoichiometry data, assuming that oxygen ions are in an O^{2-} state as following:

$$z^{+}(Ni) = 2(4+\delta) - 3(2-x) - 2x. \quad (4)$$

Comparison of the dependences presented in Figure 4b in the temperature range below T_c shows that the Ca doping results in the Ni average oxidation state increase (except for the LCNO01 sample).

This fact can be explained by considering both the defect structure features for layered nickelates and the anti-Frenkel disordering (Equation (3)) and also by taking into account oxidation reactions [52,53]. When considering the formation of both localized and delocalized electron holes, the oxidation reactions for this case can be written as follows:

$$\frac{1}{2}O_2 + V_i^{\times} + 2Ni_{Ni}^{\times} \leftrightarrow O_i'' + 2Ni_{Ni}^{\bullet}, \quad (5)$$

$$\frac{1}{2}O_2 + V_i^{\times} \leftrightarrow O_i'' + 2h^{\bullet}, \quad (6)$$

where $Ni_{Ni}^{\times}$ is a Ni^{2+} cation in the regular lattice site, $Ni_{Ni}^{\bullet}$ is an electron hole localized on nickel cations (Ni^{3+}) and $h^{\bullet}$ is a delocalized electron hole, respectively.

At temperatures below T_c the oxygen non-stoichiometry values are almost constant, which can be explained by the establishment of dynamic equilibrium according to Equation (3). For calcium as an acceptor dopant, the oxidation reaction can be written with the following electroneutrality conditions:

$$2[O_i''] + [Ca_{La}'] \leftrightarrow [Ni_{Ni}^{\bullet}] + 2[V_O^{\bullet\bullet}]. \quad (7)$$

Thus, replacement with Ca^{2+} cations in the Ln^{3+} sites in the LCNO series, except for LCNO01, leads to an increase in concentration of compensating electron holes and the Ni average oxidation state. For the LCNO01 sample, the tendency for decreasing compensating electron holes due to a lesser δ value in comparison with that for the LNO sample dominates over the trend for the holes' concentration to increase due to Ca doping.

Release of the interstitial oxygen at temperatures above T_c leads to a partial annihilation of electron holes due to the reduction of Ni^{3+} to Ni^{2+} (Figure 4b). However, such a decrease is not significant for the heavily doped samples.

3.3. Structural Changes in $La_{2-x}Ca_xNiO_{4+\delta}$ under Heating in Air

Figure 5 demonstrates Ca content dependences of the unit cell parameters and volume for the LCNO series after the treatment in He (pO_2 = 0.02) and in He+O_2 (pO_2 = 0.2). The unit cell parameters' mismatch after the treatment is greater for the samples with lower Ca content and gradually decreases with an increase in Ca content. The mismatch is almost negligible for the LCNO04 sample. Provided that the change in the values is caused by the excess interstitial oxygen loss, this data agrees well with the above-mentioned decrease in the oxygen over-stoichiometry (δ) with the Ca content being increased.

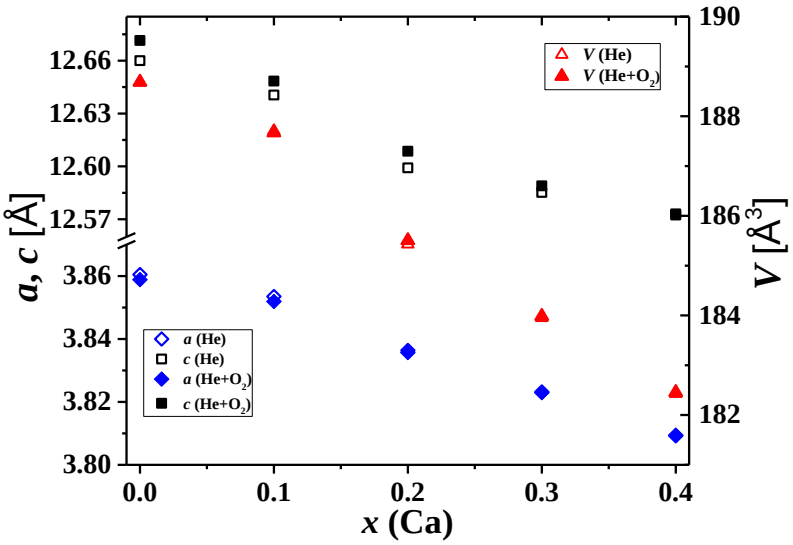

Figure 5. Concentration dependences of the unit cell parameters and volumes for the $La_{2-x}Ca_xNiO_{4+\delta}$ samples after sequential treatment under atmospheres with high and low pO_2. XRD data obtained at the anomalous scattering station (SSRTC, Novosibirsk) at a wavelength of 0.15402 nm.

Temperature dependences of the unit cell parameters and the volume obtained in the He+O_2 gas mixture (at pO_2 equal to 0.2) for the LNO and LCNO01-04 samples pretreated in He are displayed in Figure 6a–e. All the doped samples demonstrate anisotropic, high-temperature behavior for *a* and *c* parameters, similar to that of the parent LNO structure. At temperatures higher than 330 °C, opposite deviations from the linear behavior were observed for unit cell parameters *a* and *c*, both for cooling and heating stages. This pattern we assume to be caused by the over-stoichiometric oxygen loss/uptake. The reason for this anisotropic behavior is the removal of interstitial oxygen and the reduction of Ni ions. While this causes shortening of average La/Ca-O distance and thickness of the rock salt layer, it also extends the average Ni-O bond length, thus expanding the structure [54]. It is also worth mentioning that this chemical contribution to the thermal expansion has a compensating effect, and the unit cell volumes exhibit a nearly linear behavior over the entire temperature range. The most pronounced effect was observed for the LNO, LNCO01 and LNCO02 samples, while that for the LNCO04 sample was almost negligible, and this agrees well with the oxygen stoichiometry change (Figure 4). T_{cXRD} values are also close to those obtained from the TGA data (in the case of the XRD data, T_{cXRD} values are related to the intersection points of the linear interpolation at low-temperature and high-temperature regions on the curves). There were no phase transitions near the T_{cXRD} temperatures for all the samples. The phase transition from an orthorhombic to a tetragonal structure for LNO was not observed up to 700 °C (Figure S7). The hysteresis for the cell parameters before/after heating correlates with the amount of oxygen lost during pretreatment in He. Ca^{2+} has a slightly smaller ionic radius of 1.18 Å compared to 1.22 Å of La^{3+} [39], thus having a minor steric effect on the RP lattice.

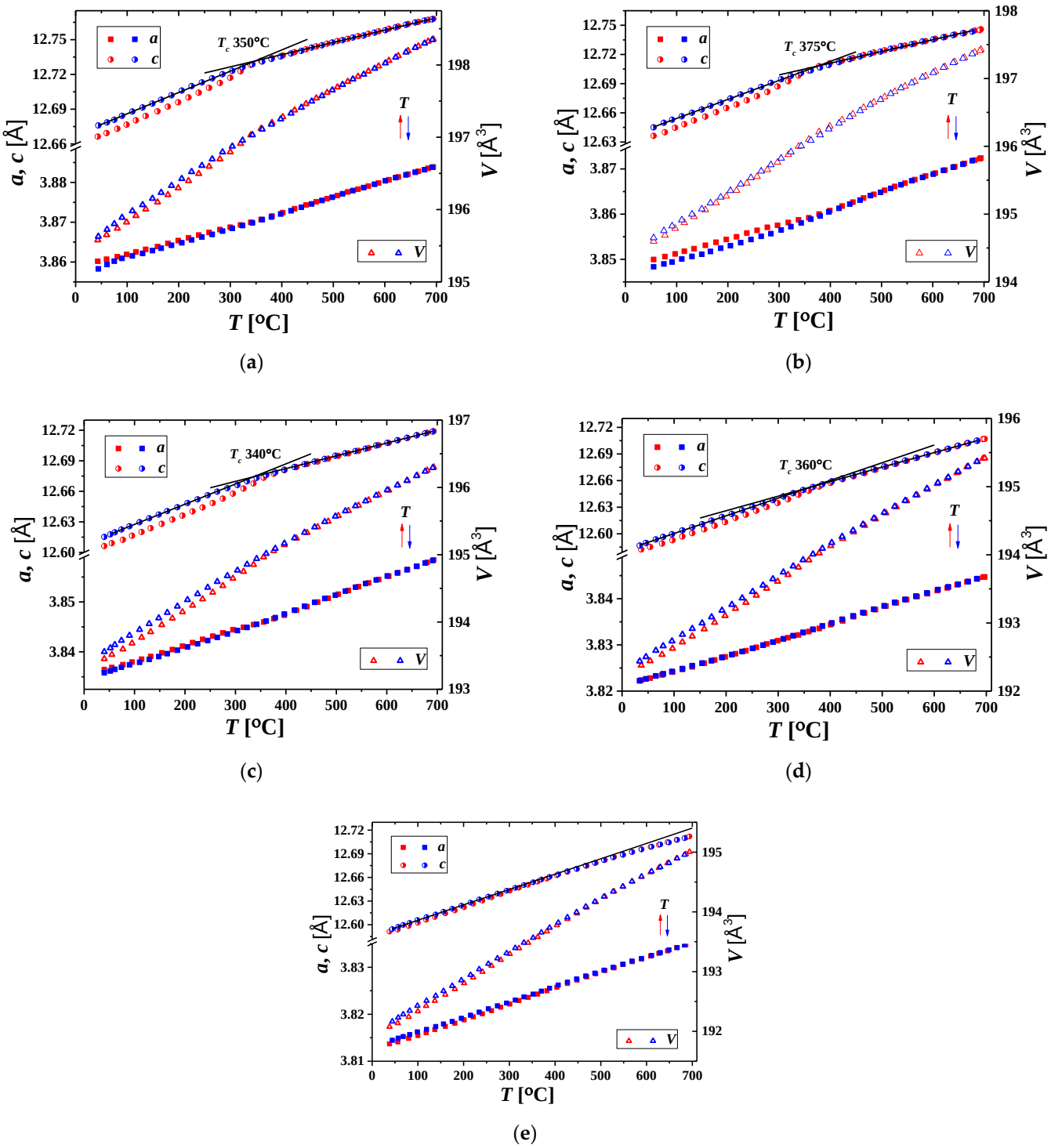

Figure 6. Temperature dependences of the unit cell parameters and volumes for the samples: $La_2NiO_{4+\delta}$ (**a**), $La_{1.9}Ca_{0.1}NiO_{4+\delta}$ (**b**) $La_{1.8}Ca_{0.2}NiO_{4+\delta}$ (**c**), $La_{1.7}Ca_{0.3}NiO_{4+\delta}$ (**d**) and $La_{1.6}Ca_{0.4}NiO_{4+\delta}$ (**e**) collected in synthetic air. Black lines are the linear approximations for the *c* parameter (cooling mode) in the temperature ranges of 50–250 °C and 500–700 °C. Red and blue symbols represent the heating and cooling modes, respectively. In Situ XRD data were obtained at the precision diffractometry-2 station (SSRTC, Novosibirsk) at a wavelength of 0.101 nm.

3.4. Oxygen Mobility and Surface Reactivity

According to the TPIE data for the LNO and LCNO01-04 samples (Figure S8, Supplementary Materials), the oxygen exchange process is initiated at ~200–400 °C depending

on the Ca content: Increasing the Ca content results in the TPIE curves shifting towards higher temperatures. For the LNO and LCNO01-03 samples, almost all the bulk oxygen was involved in the exchange during the TPIE run, while its fraction (extent of exchange) was only 70% for the LCNO04 sample (Figure S9, Supplementary Materials). Such a tendency for the extent of the exchange to decrease while the Ca content is increased qualitatively demonstrates a reduction in oxygen mobility that is typical for Ca-doped Ln nickelates [8,21,41,55]. The presence of two or more peaks on the TPIE curves reveals the non-uniformity of oxygen diffusivity.

According to the TPIE data modeling, oxygen diffusivity in the LNO sample obtained by the organic-nitrate combustion method in the current study with the final synthesis temperature of 1100 °C was significantly higher compared to that for the LNO sample obtained by the solid-state reaction method at 1250 °C in [21]. Data being equal for both samples obtained under experimental conditions are shown in Figure S10 in the Supplementary Materials. Oxygen tracer diffusion coefficient and surface heteroexchange rate values are given in Table 2 and plotted in Figure 7.

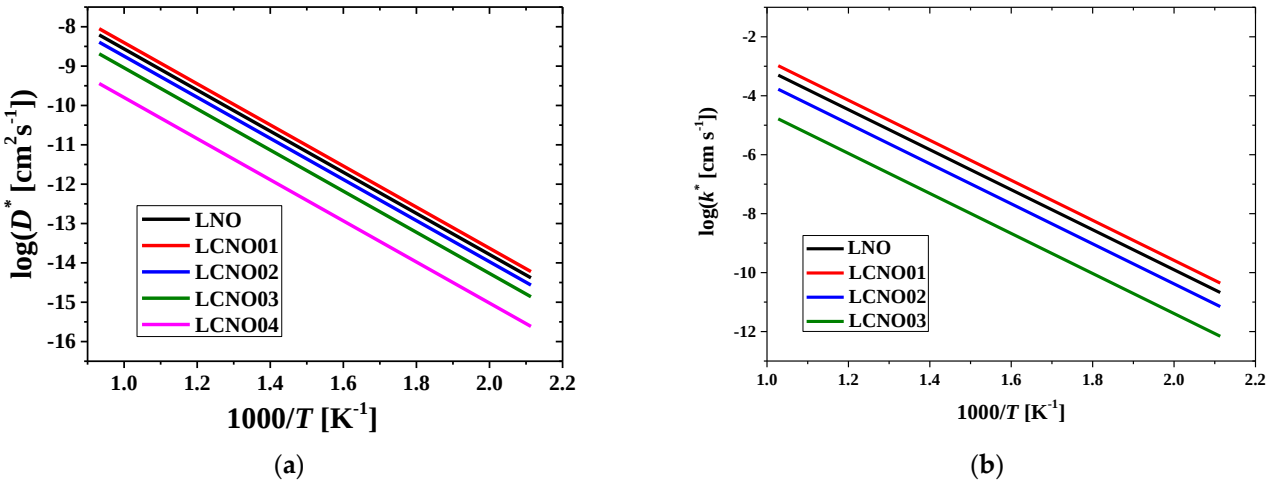

Figure 7. Arrhenius plots for the oxygen tracer diffusion coefficient (**a**) and surface exchange constant (**b**) values for the $La_{2-x}Ca_xNiO_{4+\delta}$ samples according to the TPIE with $C^{18}O_2$ data.

As follows from Table 2 and Figure 7a, D^* values are high for the LNO and LCNO01-03 samples (6.5×10^{-10}–2.8×10^{-9} cm^2 s^{-1} at 700 °C, Table 2). This is related to the cooperative mechanism of oxygen migration with the participation of both regular and highly mobile interstitial oxygen [8,23,24]. However, they are slightly lower than those for Pr and Nd nickelates: For comparison, $D^* = 7.0 \times 10^{-8}$ cm^2 s^{-1}, 7.6×10^{-10} cm^2 s^{-1}, 4.5×10^{-8} cm^2 s^{-1} and 6.3×10^{-10} cm^2 s^{-1} at 700 °C for $Pr_2NiO_{4+\delta}$, $Pr_{1.7}Ca_{0.3}NiO_{4+\delta}$, $Nd_2NiO_{4+\delta}$ and $Nd_{1.7}Ca_{0.3}NiO_{4+\delta}$, respectively [21,41,55], which can be associated with the larger ionic radius of La^{3+} compared to those for Pr^{3+} and Nd^{3+} [8,39]. It is interesting that, differing from oxygen diffusivity data reported in [32,56], the oxygen mobility and surface reactivity for LCNO01 obtained in this study were higher compared to those for LNO, which differs from tendencies for Ca-doped Pr and Nd nickelates [41,55]. However, such an increase in the oxygen mobility for low x values concurs with the data presented in [29]. In [29], it is attributed to an increase in mobility caused by a change in activation energy that is connected with the expansion of the La–O2 bond length, providing a larger space for the oxygen anions' migration and thus improving their mobility. In this work, the La/Ca–O2x1 bond length was insignificantly higher for the LCNO01 sample compared to that for the LNO sample (Figure 3b). Next, a shortening of this bond length was observed as the Ca content was increased, which would imply a correlation between the La/Ca–O2x1 bond length and oxygen diffusivity. However, the activation energy was the same for all samples (Table 2). Hence, the increase of oxygen mobility for low x values is probably generally associated with the smaller Ca^{2+} cation radius compared to that

of the host cation (as well as higher La/Ca–O2x1 bond length) [39]. It is interesting that such a tendency correlates with that demonstrated for the chemical diffusion coefficient for $La_{2-x}Ca_xNiO_{4+\delta}$ (x = 0–0.2), with a maximum for x = 0.1 [22]. However, it is to be noted that direct comparison of the values of the oxygen tracer diffusion coefficient and the chemical diffusion coefficient may not be valid.

Table 2. Oxygen heteroexchange reaction with a rate R, oxygen diffusion (normalized on particle size) via fast channel with a coefficient D^* and their effective activation energies (E_R, E_D) for $La_{2-x}Ca_xNiO_{4+\delta}$.

x	$R\|_{700\ K}$, [min^{-1}]	E_R, [kJ mole^{-1}]	$(D^*\|_{700\ K})/L^2$, [min^{-1}]	$D^*\|_{700\ °C}$, [cm^2 s^{-1}]	E_D, [kJ mole^{-1}]	Method	Ref.
0	2.4×10^3	130	0.8 (100%) *	2.0×10^{-9}	100	TPIE $C^{18}O_2$	This work
0				3.38×10^{-8}	82	IEDP/SIMS	[20,57]
0				5.5×10^{-10}	100	TPIE $C^{18}O_2$	[21]
0				1.0×10^{-8}	130	IIE $^{18}O_2$	[28,32]
0.1	5×10^3	130	1.2 (100%) *	2.8×10^{-9}	100	TPIE $C^{18}O_2$	This work
0.1				1.8×10^{-10}	160	IIE $^{18}O_2$	[32]
0.2	8×10^2	130	0.6 (85%) *	1.3×10^{-9}	100	TPIE $C^{18}O_2$	This work
0.3	8×10^1	130	0.4 (60%) *	6.5×10^{-10}	100	TPIE $C^{18}O_2$	This work
0.3				1.5×10^{-9}	100	TPIE $C^{18}O_2$	[21]
0.4	Not det **		0.06 (5%) *	1.1×10^{-10}	100	TPIE $C^{18}O_2$	This work

* θ_{fast}, fraction of oxygen involved in fast diffusion channel (in [%]). ** diffusion is limiting.

For the LCNO02-04 samples, the D^* values decrease as the Ca content increases. However, the effective activation energy values for both the diffusion coefficient and the exchange rate do not depend on the Ca content (Table 2). This may be related to a reduction in highly mobile interstitial oxygen content as a charge compensation mechanism [8,19,21,28,32,41,55–57] as was demonstrated by the XRD and TGA data (Sections 3.1–3.3). This implies that the dominating mechanism of oxygen transport is maintained for LNO and LCNO01-03. Irrespective of this, D^* and $E_{a,D}$ values are comparable to those given in other works for Ca-doped La nickelates (Table 2) [20,21,28,32,57]. For the LCNO04 sample, a "slow diffusion" mechanism predominates. Such a mechanism is probably associated with a slow exchange between the most mobile oxide anions and neighboring oxide anions [36], most likely in the perovskite layers (as will be indicated below). This is implied by significant difference in the TPIE curves for the LCNO04 sample (generally, high-temperature exchange during the TPIE run) and the other samples (low–intermediate temperature-activated diffusion) (Figure S8) as well as a small fraction of oxygen involved in "fast" diffusion (Table 2).

A similar tendency was demonstrated for the oxygen heteroexchange rate and surface exchange constant (Table 2, Figure 7b). This could be caused by the overall oxygen mobility increasing due to both the reduction of the interstitial oxygen concentration and an increase in the La_2O_2 layer thickness (the space for the oxygen movement) at x = 0.1. For the LCNO02-04 samples, the decrease in k^* and D^* kinetic parameters that occurs when the Ca content is increased may be associated with difficulties in the surface exchange process, which are possibly due to steric factors as well as a lower coverage caused by the formation of carbonates on the active sites of the surface enriched with excess calcium [41]. The other probable reason is Ca segregation on the surface blocking La–O centers [32].

For the LCNO02-04 samples, a certain non-uniformity of oxygen diffusivity was revealed. To describe such a non-uniformity, the mathematical model presented in [36] was used (schematically shown in Figure S11). Such non-uniformity as was observed during the TPIE run can be defined by the relatively fast diffusion via a cooperative mechanism in the low and intermediate temperature range with a subsequent slower exchange of the most mobile oxide anions with more strongly bound adjacent anions of the O sublattice in the high temperature range. The other reason may be associated with the features of the synthesis technique, as for example, the solid-state route can lead to inhomogeneity in the powders obtained [28]. In this study, the powders were obtained using the solution-assisted technique, which allowed a more homogeneous distribution

of elements in the materials that were obtained. The phenomenon of non-uniformity of oxygen diffusivity was not observed in the considered dopant's concentration range (x = 0.1–0.4) for Ca-doped Nd and Pr nickelates synthesized using various solution-assisted techniques [21,41,55]. The slow exchange can be described by a coefficient β with values of 0.06, 0.01 and 0.0006 min^{-1} for the LCNO02-04 samples, respectively, and the effective activation energy of 80 kJ $mole^{-1}$. It is interesting that non-uniformity of oxygen bulk diffusivity was observed for the $La_{2-x}Ca_xNiO_{4+\delta}$ samples at a lower Ca content compared to that for $Pr_{2-x}Ca_xNiO_{4+\delta}$ and $Nd_{2-x}Ca_xNiO_{4+\delta}$. In the $Pr_{2-x}Ca_xNiO_{4+\delta}$ series, non-uniformity was observed at $x \geq 0.4$, while in the $Nd_{2-x}Ca_xNiO_{4+\delta}$ series, it was not observed in the range of $0.0 \leq x \leq 0.4$. These facts can be related to both the cation size effect and the interstitial oxygen content as well as other probable reasons such as the ability to form oxygen vacancies in perovskite layers, Ln/Ca–O and Ni–O bonds' length, the facility of oxide anions to jumps through $Ln_{3-x}Ca_x$ triangles, configuration of rock salt and perovskite layers, etc. [8,19,21,41,55].

Nevertheless, with Ca doping, the oxygen tracer diffusion coefficient and surface heteroexchange rate values remain sufficiently high for the LCNO01-03 samples, with the best performance coming from LCNO01, to make these materials attractive for their application in solid oxide fuel cell air electrodes and MIEC membranes for oxygen separation and syngas production [8,58,59].

3.5. Electrochemical Study of the $La_{2-x}Ca_xNiO_{4+\delta}$ Electrodes

Figure 8a,b shows the results of studies of the electrochemical activity of the LNO and LCNO01-04 based electrodes in symmetric cells. Examples of the electrode microstructure are shown in Figure S12. The specific surface area of the electrode powders showed the tendency to increase with Ca doping (Table S1). This agrees well with the data presented in [29], wherein the negative influence of Ca doping on the sintering properties of $La_{2-x}Ca_xNiO_{4+\delta}$ ceramics was demonstrated. In the functional layers, after the sintering, an increase in the average size of particles was observed (Table S3). Despite some difference in the powder's dispersity and materials' sinterability, all the electrodes showed excellent adhesion to the SDC substrate.

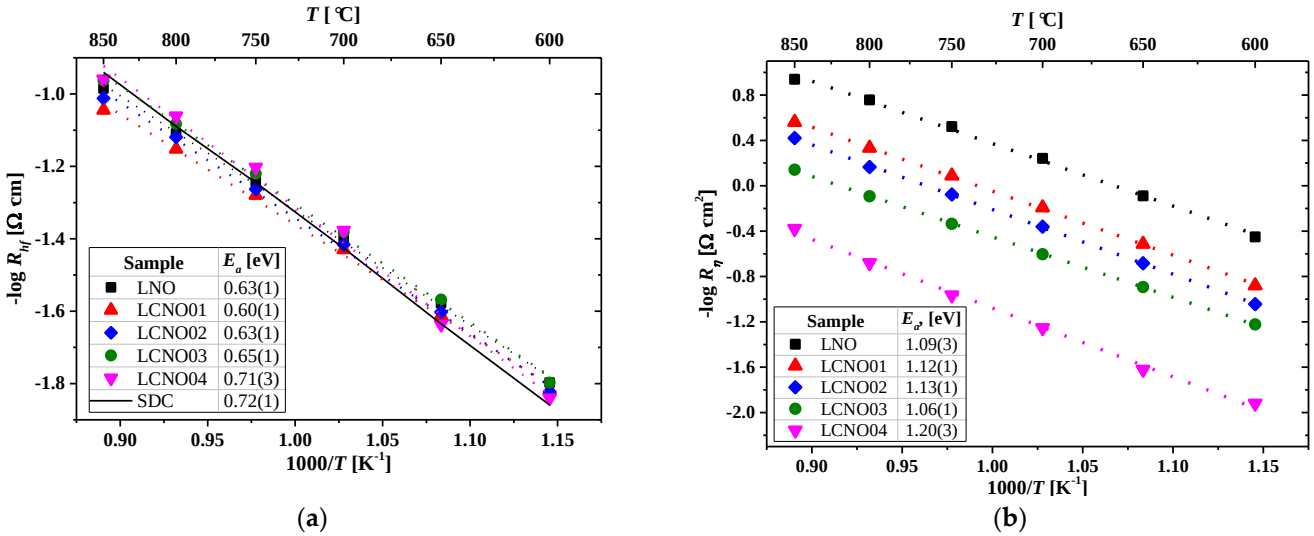

Figure 8. Temperature dependences of the reciprocal serial R_{hf} (**a**) and polarization R_η (**b**) resistance of the $La_{2-x}Ca_xNiO_{4+\delta}$ electrodes in air.

Ca doping had no significant effect on the serial resistance value (R_{hf}) (Figure 8a), which was determined from the high-frequency intercept of the spectra with the real axis in the Nyquist coordinates. It is commonly accepted that the serial resistance, in addition to the electrolyte substrate ohmic resistance, may include a parasitic resistance in the cell due to metallic contacts and interface components of the electrode/electrolyte interaction [9].

Across the entire series, the R_{hf} and activation energy E_a were approximately equal and close in value to the ohmic resistance and E_a of the SDC electrolyte. This means that the resistance of the electrolyte provides the main contribution to the R_{hf} values.

The dependences of the reciprocal polarization resistance R_η (polarization conductivity of the electrodes) clearly demonstrate a decrease in the electrochemical activity of the electrodes with an increase in Ca content. Thus, the values of the R_η of the electrodes measured at 700 °C increased in the series 0.57 (LNO) < 1.56 (LCNO01) < 2.30 (LCNO02) < 4.01 (LCNO03) < 17.94 (LCNO04) Ω·cm^2. However, the values of the activation energy of the polarization conductivity changed insignificantly for LNO-LCNO03, and only for the LCNO04 sample was a visible E_a increase observed along with the highest R_η in the series, exceeding other values by a factor of 4–9.

To elucidate the reasons for such behavior from the electrodes, the impedance spectra for the LNO-LCNO03 electrodes were analyzed using ZView software. Figure 9 presents the normalized impedance spectra measured at 700 °C in air. The R_{hf} resistance was subtracted from the data set. All the spectra have the shape of asymmetric deformed semicircles, similar to the Gerischer impedance, and are well described by the Gerischer element connected in series with the (RQ) element, i.e., a parallel combination of a resistance and a CPE (constant phase element or Q-element: $Y_Q(w) = (Q(jw)^n)^{-1}$), which correlates well with [60,61]. When using this equivalent circuit, the calculation error did not exceed 3–5%. The characteristic capacitance of the high-frequency (RQ) process is $C_1 \sim 10^{-2}$ F·cm^{-2}, and the frequency power dependence (n) of this CPE is approximately 0.5, which indicates that it is most likely related to a diffusion process. The Gerischer resistance makes a larger contribution to the polarization resistance; therefore, it can be assumed that the behavior of the electrodes is due to the diffusion impedance.

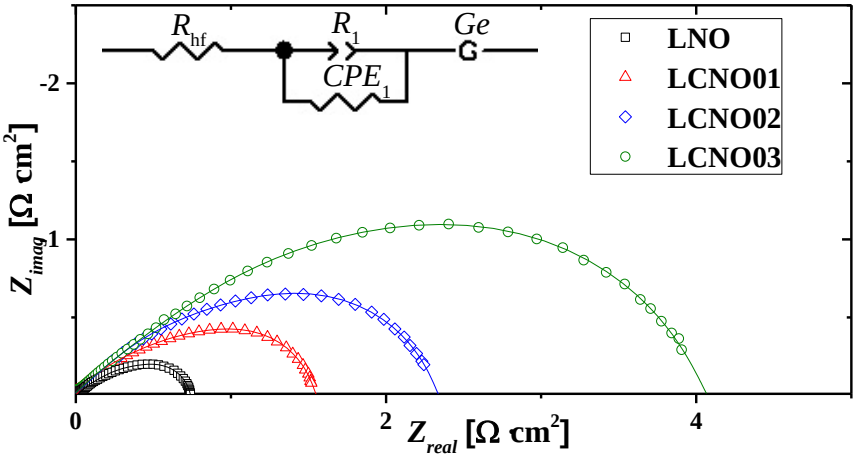

Figure 9. Typical Nyquist plots of impedance, obtained at 700 °C in air with electrolyte resistance subtracted.

The Gerischer impedance [62,63] or in other words, the chemical impedance [64,65], is often used for fitting the spectra of the electrodes based on mixed ionic and electronic conductors (MIEC):

$$Y_G = Y_0\sqrt{K_G + jw} = \frac{\sqrt{K_G + jw}}{R_G\sqrt{K_G}} \quad (8)$$

where Y_0 is the Gerischer admittance being proportional to $\sqrt{D}$, K_G is the Gerischer time constant being proportional to $\sqrt{K}$, which corresponds to the rate of reaction of transforming mobile particles into immobile/inactive species or forming electrochemically inactive complexes, and w is the angular frequency, $w = 2\pi f$.

According to the Adler–Lane–Steele model, the polarization resistance of the electrodes is influenced by many factors such as the electrode microstructure and transport properties of the electrode material [63–70]. According to mathematical transformations

presented in [63,66], the equation for the Gerischer impedance can be written in the following form:

$$R_{chem} = \frac{RT}{4F^2}\sqrt{\frac{\tau}{(1-\varepsilon)4ac_0^2D^*k^*}};\ K_G = \frac{4aA_0k^*}{(1-\varepsilon)x_v^0} \quad (9)$$

where R is the universal gas constant; F is the Faraday constant; ε is the electrode porosity; τ is the solid phase tortuosity; a is specific surface area; c_0 is molar concentration of the structural oxygen; x_v^O is the oxygen vacancies (in this case, interstitial oxygen) mole fraction; A_0 is the thermodynamical factor, which is described as a function of oxygen nonstoichiometry on pO_2; and k^* and D^* are the oxygen surface exchange constant and tracer diffusion coefficient.

Thus, for other conditions of the electrode preparation being equal, considering the electrodes' morphological characteristics as being similar across the entire series and assuming that the other parameters (A_0, c_0, x_v^O) do not contribute significantly to the dependence qualitative behavior, a qualitative correlation of the polarization resistance (R_η) and kinetic parameters (k^*, $D_{eff}{}^*$) can be estimated as an inverse proportion of $\sqrt{k^*D^*_{eff}}$. A similar approach was successfully applied in [21,41,63,69] to establish a correlation between the transport properties of Pr and Nd nickelates and the electrochemical characteristics of the related electrodes.

The effective oxygen tracer diffusion coefficient $D_{eff}{}^*$ can be estimated as $\theta_{fast}D^*$, where θ_{fast} is the fraction of oxygen involved in a fast diffusion channel with the coefficient D^* (Table 2). The oxygen surface exchange constant k^* can be evaluated from the oxygen isotope exchange data using the oxygen heteroexchange rate R values as follows:

$$k^* = R\frac{V_{sample}}{N_{bulk}}, \quad (10)$$

where V_{sample} and N_{bulk} are the sample volume and the number of oxide anions in the sample bulk [69,71]. To compare the electrochemical data obtained in the air atmosphere and the TPIE data obtained in the 1 vol.% CO_2-containing atmosphere, the k^* values should be recalculated. It has been shown for the Pr nickelate perovskites that the k^* values for the exchange with $C^{18}O_2$ were 2 orders of magnitude higher compared to the k^* values for the exchange with $^{18}O_2$, with the effective activation energy values for these processes differing insignificantly [72]. The effective order with respect to the oxygen containing gas may vary within the range of ~0.5–1 for both dioxygen [73,74] and carbon dioxide [73,75]. The pseudo-first order was used in this study.

The correlation of R_η and $k^*D_{eff}{}^*$ is linear. This fact demonstrates the important role of the oxygen transport characteristics of the MIEC material in determining the performance of the related MIEC electrodes. It was established in several studies that Ca doping results in the total conductivity in the $La_{2-x}Ca_xNiO_{4+\delta}$ series [9,22,28] increasing. Heavily doped samples (x = 0.2–0.5) have a conductivity level of 120–165 S cm^{-1} compared to 60–70 S cm^{-1} for the undoped LNO (at 700 °C), which is expected to have a positive effect on the performance of the electrodes. However, the ionic conductivity decreases at $x \geq 0.2$ [29] and, as has been revealed in the current study, the coefficient D^* values gradually reduce at $x \geq 0.2$, showing a sharp fall at x = 0.4. The last-mentioned factors seem to have the determining influence on the performance of the electrodes being considered in this study with the application of a highly conductive collector (LNF conductivity reaches 200–700 S cm^{-1} depending on the porosity [65]). In the case of the electrodes not having a collecting layer, it is probable that all factors will have a competing effect on the electrode activity.

As seen from Figure 10, the following dependences $R_{q,G} \sim \left(\sqrt{k^*D^*_{eff}}\right)^{-1}$, $K_G \sim R$, $Y_o \sim \sqrt{D^*_{eff}}$ can be observed between the parameters obtained by different research methods—electrochemical impedance spectroscopy and isotope exchange study. The

general tendency (except for $La_{1.9}Ca_{0.1}NiO_{4+\delta}$) of increasing impedance characteristics and decreasing isotope exchange parameters with increasing Ca content can be observed. This concurs with the dependences derived from Equation (9) and allows us to conclude that the diffusion impedance of the electrodes based on $La_{2-x}Ca_xNiO_{4+\delta}$ depends on the kinetic parameters of k^* and D_{eff}^*. An exception to this is the electrode with $x = 0.1$, which shows slightly higher polarization resistance compared to the LNO electrode despite its superior oxygen transport properties. The probable reason for this contradiction is the non-optimized microstructure of the electrode. It was shown that a parameter such as tortuosity of the electrode layer along with its porosity may have had an influence on the electrode performance [76,77]. Moreover, while the powders used in isotope exchange studies were sintered at 1150 °C with subsequent ball milling, which could generate extended defects providing fast oxygen migration channels in these complex oxides [50,72], their layers supported on electrolytes were additionally sintered at 1250–1200 °C, thus apparently annealing defects and leading to some segregation of Ca cations on the surface of pores and decreasing oxygen mobility and surface reactivity. Such phenomena could not be substantial for more heavily doped samples with inherently worse transport properties while being detectable for the sample with the lowest amount of dopant.

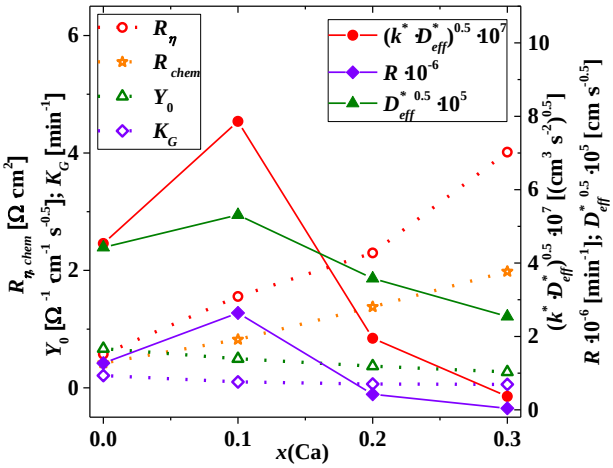

Figure 10. Correlation between the EIS data such as polarization R_η, Gerischer R_G resistance, Gerischer admittance Y_0, Gerischer time constant K_G and the isotopic exchange kinetic parameters $k^*D_{eff}^*$, oxygen heteroexchange rate R, tracer diffusion coefficient D_{eff}^*.for the $La_{2-x}Ca_xNiO_{4+\delta}$ series at 700 °C in air.

Summarizing, it should be noted that in a recent study performed on a button cell with a proton-conducting $BaZr_{0.3}Ce_{0.5}Y_{0.2}O_3$ electrolyte [22], it was shown that the use of an optimized LCNO01 electrode resulted in 30.5% higher performance compared to that of an LNO electrode and allowed a very low polarization resistance (0.102 Ω cm^2 at 700 °C) to be obtained. Hence, to implement the potentiality of the LCNO01 material possessing superior oxygen transport properties, future study should be directed to optimization of the electrode layers' features and investigation of their performance and stability both in symmetrical and button cells.

4. Conclusions

In this work, the $La_{2-x}Ca_xNiO_{4+\delta}$ oxides ($x = 0$–0.4) were studied from the perspective of their use as materials for oxygen separation membranes and for intermediate temperature Solid oxide fuel cell/Solid oxide electrolysis cell's air electrodes. The materials were synthesized via a nitrate combustion method and characterized by XRD studies at room temperature as well as at high temperatures, TGA, DSC and also by temperature-programmed isotope exchange of oxygen with $C^{18}O_2$ in a flow reactor. $La_{2-x}Ca_xNiO_{4+\delta}$ samples were single-phase oxides with *Fmmm* space group for $x = 0$ and *I4/mmm* for

x = 0.1–0.4. Changes in the unit cell parameters and volume during heating and cooling were shown to have been caused by the excess oxygen loss. A high oxygen mobility and surface reactivity was demonstrated for $La_{2-x}Ca_xNiO_{4+\delta}$ samples for x = 0.1–0.3 due to the cooperative mechanism of oxygen migration involving both regular and highly-mobile interstitial oxygen, while poor oxygen kinetic properties for the sample with x = 0.4 could be characterized by the predominance of slow exchange between the oxide anions in closest proximity to each other. Typically for Ruddlesden–Popper phases, oxygen mobility and surface reactivity decrease with increasing Ca content due to a decrease in the highly mobile interstitial oxygen content as a charge compensation mechanism. The exception for x = 0.1 is probably related to the smaller Ca^{2+} cation radius compared to that of host La^{3+}, as well as other features such as an insignificant increase in La/Ca–O2x1 bond length and improving the transport of interstitial oxide anions with a small reduction in the over-stoichiometric oxygen content due to the increasing mobility of interstitial oxide anions at a low Ca-doping level. For the samples with $x \geq 0.2$, a certain non-uniformity of oxygen diffusivity was revealed: fast diffusion via cooperative mechanisms and slow diffusion via exchange of the most mobile oxide anions with more strongly bound neighboring anions. The electrochemical performance of symmetric cells with electrodes based on $La_{2-x}Ca_xNiO_{4+\delta}$ was studied by an electrochemical impedance spectroscopy method. The performances of the LCNO01-03 electrodes were lower than that of the LNO electrode, which correlated with the oxygen transport properties (oxygen tracer diffusion coefficient and surface exchange constant) specified in the Adler–Lane–Steele model. Further modification in the electrode microstructure is necessary, as well as a comprehensive investigation of its correlation with electrochemical properties in order to clarify the achievable maximum performance of electrodes based on doped materials, especially for LCNO01, which possesses superior oxygen transport properties compared to undoped LNO.

Supplementary Materials: The following are available online at https://www.mdpi.com/2073-4352/11/3/297/s1.

Author Contributions: Conceptualization, E.P. and V.S.; methodology, E.S. and A.K.; software, A.K.; validation, E.P., N.Y., and Z.V.; formal analysis, E.S. and A.K.; investigation, D.M., Z.V., N.Y., A.K.; resources, E.P.; writing—original draft preparation, N.Y., E.F., Z.V. and A.K.; writing—review and editing, E.P. and V.S.; visualization, E.F., D.M., N.Y., A.K.; supervision, E.P., V.S. and A.S.; project administration, E.P., A.S. and V.S.; data curation and investigation, V.B. All authors have read and agreed to the published version of the manuscript.

Funding: This research received no external funding.

Institutional Review Board Statement: Not applicable.

Informed Consent Statement: Not applicable.

Data Availability Statement: All data presented in the main text and Supplementary materials are fully available without restriction.

Acknowledgments: The materials synthesis as well as electrochemical study were performed in a framework of the budget task of the IHTE UB RAS with using the equipment of the shared access center "Composition of compounds". The TGA and isotope exchange studies were supported by the Ministry of Science and Higher Education of the Russian Federation within the governmental order for Boreskov Institute of Catalysis (projects AAAA-A21-121011390007-7, AAAA-A21-121011390009-1). The SXRD experiments were performed at the shared research center SSTRC on the basis of the Novosibirsk VEPP-3 complex at BINP SB RAS, using equipment supported by project RFMEFI62119X0022.

Conflicts of Interest: The authors declare no conflict of interest.

References

1. Nirala, G.; Yadav, D.; Upadhyay, S. Ruddlesden–Popper phase A_2BO_4 oxides: Recent studies on structure, electrical, dielectric, and optical properties. *J. Adv. Ceram.* **2020**, *9*, 129–148. [CrossRef]
2. Istomin, S.Y.; Antipov, E.V. Cathode materials based on perovskite-like transition metal oxides for intermediate temperature solid oxide fuel cells. *Russ. Chem. Rev.* **2013**, *82*, 686–700. [CrossRef]
3. Kilner, J.A.; Burriel, M. Materials for intermediate-temperature solid-oxide fuel cells. *Ann. Rew. Mater. Res.* **2014**, *44*, 365–393. [CrossRef]
4. Guo, H.; Hu, Z.; Pi, T.-W.; Tjeng, L.H.; Komarek, A.C. Single crystal growth of pure Co^{3+} oxidation state material $LaSrCoO_4$. *Crystals* **2016**, *6*, 98. [CrossRef]
5. Ceretti, M.; Corallini, S.; Paulus, W. Influence of phase transformations on crystal growth of stoichiometric brownmillerite oxides: Sr_2ScGaO_5 and $Ca_2Fe_2O_5$. *Crystals* **2016**, *6*, 146. [CrossRef]
6. Zhao, H.; Li, Q.; Sun, L. Ln_2MO_4 cathode materials for solid oxide fuel cells. *Sci. China Chem.* **2011**, *54*, 898–910. [CrossRef]
7. Ogier, T.; Mauvy, F.; Bassat, J.M.; Laurencin, J.; Mougin, J.; Grenier, J.-C. Overstoichiometric oxides $Ln_2NiO_{4+\delta}$ (Ln = La, Pr or Nd) as oxygen anodic electrodes for solid oxide electrolysis application. *Int. J. Hydrogen Energy* **2015**, *40*, 15885–15892. [CrossRef]
8. Sadykov, V.A.; Sadovskaya, E.M.; Eremeev, N.F.; Skriabin, P.I.; Krasnov, A.V.; Bespalko, Y.N.; Pavlova, S.N.; Fedorova, Y.E.; Pikalova, E.Y.; Shlyakhtina, A.V. Oxygen mobility in the materials for solid oxide fuel cells and catalytic membranes (review). *Russ. J. Electrochem.* **2019**, *55*, 701–718. [CrossRef]
9. Wu, X.; Gu, C.; Cao, J.; Miao, L.; Fu, C.; Liu, W. Investigations on electrochemical performance of $La_2NiO_{4+\delta}$ cathode material doped at A site for solid oxide fuel cells. *Mater. Res. Express* **2020**, *7*, 065507. [CrossRef]
10. Kaur, P.; Singh, K. Review of perovskite-structure related cathode materials for solid oxide fuel cells. *Ceram. Int.* **2019**, *46*, 5521–5535. [CrossRef]
11. Badwal, S.P.S.; Foger, K. Solid oxide electrolyte fuel cell review. *Ceram. Int.* **1996**, *22*, 257–265. [CrossRef]
12. Zhao, H.; Mauvy, F.; Lalanne, C.; Bassat, J.; Fourcade, S.; Grenier, J. New cathode materials for ITSOFC: Phase stability, oxygen exchange and cathode properties of $La_{2-x}NiO_{4+\delta}$. *Solid State Ion.* **2008**, *179*, 2000–2005. [CrossRef]
13. Tamura, H.; Hayashi, A.; Ueda, Y. Phase diagram of $La_2Ni0_{4+\delta}$ ($0 \leq \delta \leq 0.18$) I. Phases at room temperature and phase transition above $\delta = 0.15$. *Physica* **1993**, *216*, 83–88. [CrossRef]
14. Huang, D.P.; Xu, Q.; Chen, W.; Zhang, F.; Liu, H.X. Sintering, microstructure and conductivity of $La_2NiO_{4+\delta}$ ceramic. *Ceram. Int.* **2008**, *34*, 651–655. [CrossRef]
15. Pikalova, E.Y.; Medvedev, D.A.; Khasanov, A.F. Structure, stability, and thermomechanical properties of Ca-substituted $Pr_2NiO_{4+\delta}$. *Phys. Solid State* **2017**, *59*, 694–702. [CrossRef]
16. Pikalova, E.; Kolchugin, A.; Filonova, E.; Bogdanovich, N.; Pikalov, S.; Ananyev, M.; Farlenkov, A. Validation of calcium-doped neodymium nickelates as SOFC air electrode materials. *Solid State Ion.* **2018**, *319*, 130–140. [CrossRef]
17. Pikalova, E.; Kolchugin, A.; Bogdanovich, N.; Medvedev, D.; Lyagaeva, J.; Vedmid, L.; Ananyev, M.; Plaksin, S.; Farlenkov, A. Suitability of $Pr_{2-x}Ca_xNiO_{4+\delta}$ as cathode materials for electrochemical devices based on oxygen ion and proton conducting solid state electrolytes. *Int. J. Hydrogen Energy* **2020**, *45*, 13612–13624. [CrossRef]
18. Nakamura, T.; Takeyama, Y.; Watanabe, S.; Yashiro, K.; Sato, K.; Hashida, T.; Mizusaki, J. Oxygen nonstoichiometry, crystal structure and mechanical properties of $La_2NiO_{4+\delta}$. *ECS Trans.* **2009**, *25*, 2573–2580. [CrossRef]
19. Kharton, V.V.; Kovalevsky, A.V.; Avdeev, M.; Tsipis, E.V.; Patrakeev, M.V.; Yaremchenko, A.A.; Naumovich, E.N.; Frade, J.R. Chemically induced expansion of $La_2NiO_{4+\delta}$-based materials. *Chem. Mater.* **2007**, *19*, 2027–2033. [CrossRef]
20. Boehm, E.; Bassat, J.; Dordor, P.; Mauvy, F.; Grenier, J.; Stevens, P. Oxygen diffusion and transport properties in non-stoichiometric $Ln_{2-x}NiO_{4+\delta}$ oxides. *Solid State Ion.* **2005**, *176*, 2717–2725. [CrossRef]
21. Pikalova, E.Y.; Kolchugin, A.A.; Sadykov, V.A.; Sadovskaya, E.M.; Filonova, E.A.; Eremeev, N.F.; Bogdanovich, N.M. Structure, transport properties and electrochemical behavior of the layered lanthanide nickelates doped with calcium. *Int. J. Hydrogen Energy* **2018**, *43*, 17373–17386. [CrossRef]
22. Li, X.; Huan, D.; Shi, N.; Yang, Y.; Wan, Y.; Xia, C.; Peng, R.; Lu, Y. Defects evolution of Ca doped $La_2NiO_{4+\delta}$ and its impact on cathode performance in proton-conducting solid oxide fuel cells. *Int. J. Hydrogen Energy* **2020**, *45*, 17736–17744. [CrossRef]
23. Li, X.; Benedek, N.A. Enhancement of ionic transport in complex oxides through soft lattice modes and epitaxial strain. *Chem. Mater.* **2015**, *27*, 2647–2652. [CrossRef]
24. Minervini, L.; Grimes, R.W.; Kilner, J.A.; Sickafus, K.E. Oxygen migration in $La_2NiO_{4+\delta}$. *J. Mater. Chem.* **2000**, *10*, 2349–2354. [CrossRef]
25. Medeiros, R.L.B.A.; Melo, V.R.M.; Melo, D.M.A.; Macedo, H.P.; Moure, G.T.; Adánez-Rubio, I.; Melo, M.A.F.; Adánez, J. Double perovskite $(La_{2-x}Ca\text{-}Ba_x)NiO_4$ oxygen carriers for chemical looping reforming applications. *Int. J. Hydrogen Energy* **2020**, *45*, 1681–1696. [CrossRef]
26. Amow, G.; Whitfield, P.S.; Davidson, I.J.; Hammond, R.P.; Munnings, C.N.; Skinner, S.J. Structural and sintering characteristics of the $La_2Ni_{1-x}Co_xO_{4+\delta}$ series. *Ceram. Int.* **2004**, *30*, 1635–1639. [CrossRef]
27. Aguadero, A.; Escudero, M.J.; Pérez, M.; Alonso, J.A.; Pomjakushin, V.; Daza, L. Effect of Sr content on the crystal structure and electrical properties of the system $La_{2-x}Sr_xNiO_{4+\delta}$ ($0 \leq x \leq 1$). *Dalton Trans.* **2006**, *36*, 4377–4383. [CrossRef]

28. Kolchugin, A.A.; Pikalova, E.Y.; Bogdanovich, N.M.; Bronin, D.I.; Pikalov, S.M.; Plaksin, S.V.; Ananyev, M.N.; Eremin, V.A. Structural, electrical and electrochemical properties of calcium-doped lanthanum nickelate. *Solid State Ion.* **2016**, *288*, 48–53. [CrossRef]
29. Shen, Y.; Zhao, H.; Liu, X.; Xua, N. Preparation and electrical properties of Ca-doped $La_2NiO_{4+\delta}$ cathode materials for IT-SOFC. *Phys. Chem. Chem. Phys.* **2010**, *12*, 15124–15131. [CrossRef] [PubMed]
30. Pikalova, E.; Bogdanovich, N.; Kolchugin, A.; Ermakova, L.; Khrustov, A.; Farlenkov, A.; Bronin, D. Methods to increase electrochemical activity of lanthanum nickelate-ferrite electrodes for intermediate and low temperature SOFCs. *Int. J. Hydrogen Energy* **2021**. [CrossRef]
31. Gilev, A.R.; Kiselev, E.A.; Zakharov, D.M.; Cherepanov, V.A. Effect of calcium and copper/iron co-doping on defect-induced properties of La_2NiO_4-based materials. *J. Alloys Compd.* **2018**, *753*, 491–501. [CrossRef]
32. Tropin, E.S.; Ananyev, M.V.; Farlenkov, A.S.; Khodimchuk, A.V.; Berenov, A.V.; Fetisov, A.V.; Eremin, V.A.; Kolchugin, A.A. Surface defect chemistry and oxygen exchange kinetics in $La_{2-x}Ca_xNiO_{4+\delta}$. *J. Solid State Chem.* **2018**, *262*, 199–213. [CrossRef]
33. FullProf Suite. Crystallographic Tools for Rietveld, Profile Matching and Integrated-Intensity Refinements of X-ray and/or Neutron Data. Available online: https://www.ill.eu/sites/fullprof/ (accessed on 26 February 2021).
34. Piminov, P.A.; Baranov, G.N.; Bogomyagkov, A.V.; Berkaev, D.E.; Borin, V.M.; Dorokhov, V.L.; Karnaev, S.E.; Kiselev, V.A.; Levichev, E.B.; Meshkov, O.I.; et al. Synchrotron radiation research and application at VEPP-4. *Phys. Procedia* **2016**, *84*, 19–26. [CrossRef]
35. Aulchenko, V.M.; Evdokov, O.V.; Kutovenko, V.D.; Pirogov, B.Y.; Sharafutdinov, M.R.; Titov, V.M.; Tolochko, B.P.; Vasiljev, A.V.; Zhogin, I.A.; Zhulanov, V.V. One-coordinate X-ray detector OD-3M. *Nucl. Instrum. Methods Phys. Res.* **2009**, *603*, 76–79. [CrossRef]
36. Sadykov, V.A.; Sadovskaya, E.M.; Filonova, E.A.; Eremeev, N.F.; Belyaev, V.D.; Tsvinkinberg, V.A.; Pikalova, E.Y. Oxide ionic transport features in Gd-doped La nickelates. *Solid State Ion.* **2020**, *357*, 115462. [CrossRef]
37. Pikalova, E.Y.; Kalinina, E.G. Approaches to improving efficiency of solid oxide fuel cells based on ceramic membranes with mixed conductivity. *Russ. Chem. Rev.* **2021**, *90*. [CrossRef]
38. Ganguly, P.; Rao, C.N.R. Crystal chemistry and magnetic properties of layered metal oxides possessing the K_2NiF_4 or related structures. *J. Solid State Chem.* **1984**, *53*, 193–216. [CrossRef]
39. Shannon, R.D. Revised effective ionic radii and systematic studies of interatomic distances in halides and chalcogenides. *Acta Cryst.* **1976**, *32*, 751–767. [CrossRef]
40. Pikalov, S.M.; Vedmid, L.B.; Filonova, E.A.; Pikalova, E.Y.; Lyagaeva, J.G.; Danilov, N.A.; Murashkina, A.A. High-temperature behavior of calcium substituted layered neodymium nickelates. *J. Alloys Compd.* **2019**, *801*, 558–567. [CrossRef]
41. Sadykov, V.A.; Pikalova, E.Y.; Kolchugin, A.A.; Filonova, E.A.; Sadovskaya, E.M.; Eremeev, N.F.; Ishchenko, A.V.; Fetisov, A.V.; Pikalov, S.M. Oxygen transport properties of Ca-doped Pr_2NiO_4. *Solid State Ion.* **2018**, *319*, 234–243. [CrossRef]
42. Shi, C.Y.; Hu, Z.B.; Hao, Y.M. Structural, magnetic and dielectric properties of $La_{2-x}Ca_xNiO_{4+\delta}$ (x = 0, 0.1, 0.2, 0.3). *J. Alloys Compd.* **2011**, *509*, 1333–1337. [CrossRef]
43. Tang, J.P.; Dass, R.I.; Manthiram, A. Comparison of the crystal chemistry and electrical properties of $La_{2-x}A_xNiO_4$ (A = Ca, Sr, and Ba). *Mater. Res. Bull.* **2000**, *35*, 411–424. [CrossRef]
44. Kim, H.S.; Yoo, H.I. Effect of acceptor size and hole degeneracy on oxygen nonstoichiometry of $La_2NiO_{4+\delta}$. *Solid State Ion.* **2013**, *232*, 129–137. [CrossRef]
45. Poirot, N.; Zaghrioui, M. Synthesis and characterization of calcium-doped lanthanium nickelates $La_{2-x}Ca_xNiO_{4+\delta}$. *Solid State Sci.* **2006**, *8*, 149–154. [CrossRef]
46. Bassat, J.M.; Odier, P.; Loup, J.P. The semiconductor-to-metal transition in question in $La_{2-x}NiO_{4+\delta}$ ($\delta > 0$ or $\delta < 0$). *J. Solid State Chem.* **1994**, *110*, 124–135.
47. Liao, Q.; Zhuang, L.; Wei, Y.; Xue, J.; Wang, H. High oxygen permeation through A-site deficient $K_2NiF_{4+\delta}$-type oxide hollow-fiber membrane. *Ceram. Int.* **2018**, *44*, 10852–10857. [CrossRef]
48. Gilev, A.R.; Kiselev, E.A.; Chezganov, D.S.; Cherepanov, V.A. Correlation between oxygen surface exchange rate and surface structure in the $La_{1.5}Sr_{0.5}Ni_{1-y}Co_yO_{4+\delta}$ ceramic membranes. *Ceram. Int.* **2020**, *46*, 17553–17560. [CrossRef]
49. Wang, J.; Zhou, J.; Yang, J.; Zong, Z.; Fu, L.; Lian, Z.; Zhang, X.; Wang, X.; Chen, C.; Ma, W.; et al. Nanoscale architecture of $(La_{0.6}Sr_{1.4})_{0.95}Mn_{0.9}B_{0.1}O_4$ (B = Co, Ni, Cu) Ruddlesden–Popper oxides as efficient and durable catalysts for symmetrical solid oxide fuel cells. *Renew. Energy* **2020**, *157*, 840–850. [CrossRef]
50. Sadykov, V.A.; Eremeev, N.F.; Usol'tsev, V.V.; Bobin, A.S.; Alikina, G.M.; Pelipenko, V.V.; Sadovskaya, E.M.; Muzykantov, V.S.; Bulgakov, N.N.; Uvarov, N.F. Mechanism of oxygen transfer in layered lanthanide nickelates $Ln_{2-x}NiO_{4+\delta}$ (Ln = La, Pr) and their nanocomposites with $Ce_{0.9}Gd_{0.1}O_{2-\delta}$ and $Y_2(Ti_{0.8}Zr_{0.2})_{1.6}Mn_{0.4}O_{7-\delta}$ solid electrolytes. *Russ. J. Electrochem.* **2013**, *49*, 645–651. [CrossRef]
51. Akbari-Fakhrabadi, A.; Toledo, E.G.; Canales, J.I.; Meruane, V.; Chan, S.H.; Gracia-Pinilla, M.A. Effect of Sr^{2+} and Ba^{2+} doping on structural stability and mechanical properties of $La_2NiO_{4+\delta}$. *Ceram. Int.* **2018**, *44*, 10551–10557. [CrossRef]
52. Gilev, A.R.; Kiselev, E.A.; Cherepanov, V.A. Synthesis, oxygen nonstoichiometry and total conductivity of $(La,Sr)_2(Mn,Ni)O_{4\pm\delta}$. *Solid State Ion.* **2015**, *279*, 53–59. [CrossRef]
53. Kim, H.-S.; Yoo, H.-I. Isothermal Onsager matrices and acceptor size effect on mass/charge transport properties of $La_{1.9}A_{0.1}NiO_{3.95+\delta}$ (A = Ca, Sr). *Phys. Chem. Chem. Phys.* **2014**, *16*, 16595–16605. [CrossRef]

54. Tarutin, A.P.; Lyagaeva, J.G.; Medvedev, D.A.; Bi, L.; Yaremchenko, A.A. Recent advances in layered $Ln_2NiO_{4+\delta}$ nickelates: Fundamentals and prospects of their applications in protonic ceramic fuel and electrolysis cells. *J. Mater. Chem.* **2021**, *9*, 154–195. [CrossRef]
55. Pikalova, E.Y.; Sadykov, V.A.; Filonova, E.A.; Eremeev, N.F.; Sadovskaya, E.M.; Pikalov, S.M.; Bogdanovich, N.M.; Lyagaeva, J.G.; Kolchugin, A.A.; Vedmid, L.B.; et al. Structure, oxygen transport properties and electrode performance of Ca-substituted Nd_2NiO_4. *Solid State Ion.* **2019**, *335*, 53–60. [CrossRef]
56. Cherepanov, V.A.; Gilev, A.R.; Kiselev, E.A. Electrotransport in the La_2NiO_4-based solid solutions. *Pure Appl. Chem.* **2019**, *91*, 911–922. [CrossRef]
57. Skinner, S.J.; Kilner, J.A. Oxygen diffusion and surface exchange in $La_{2-x}Sr_xNiO_{4+\delta}$. *Solid State Ion.* **2000**, *135*, 709–712. [CrossRef]
58. Sadykov, V.A.; Arapova, M.V.; Smal, E.A.; Pavlova, S.N.; Bobrova, L.N.; Eremeev, N.F.; Mezentseva, N.V.; Simonov, M.N. Nanocomposite Catalysts for Transformation of Biofuels into Syngas and Hydrogen: Fundamentals of Design and Performance, Application in Structured Reactors and Catalytic Membranes. In *Catalysis*; Spivey, J., Han, Y., Shekhawat, D., Eds.; Royal Society of Chemistry: London, UK, 2019; Volume 31, pp. 216–241.
59. Gilev, A.R.; Kiselev, E.A.; Malyshkin, D.A.; Sukhanov, K.S.; Cherepanov, V.A. Hydration effect on properties of the $La_{2-x}A_xNi_{1-y}Fe_yO_{4+\delta}$ (A = Ca, Sr) cathode materials for H^+-SOFCs. *J. Alloys Compd.* **2021**, *860*, 158482. [CrossRef]
60. Hildenbrand, N.; Nammensma, P.; Blank, D.H.A.; Bouwmeester, H.J.M.; Boukamp, B.A. Influence of configuration and microstructure on performance of $La_2NiO_{4+\delta}$ IT-SOFC cathodes. *J. Power Source* **2013**, *238*, 442–453. [CrossRef]
61. Antonova, E.P.; Khodimchuk, A.V.; Usov, G.R.; Tropin, E.S.; Farlenkov, A.S.; Khrustov, A.V.; Ananyev, M.V. EIS analysis of electrode kinetics for $La_2NiO_{4+\delta}$ cathode in contact with $Ce_{0.8}Sm_{0.2}O_{1.9}$ electrolyte: From DRT analysis to physical model of the electrochemical process. *J. Solid State Electrochem.* **2019**, *23*, 1279–1287. [CrossRef]
62. Boukamp, B.A.; Bouwmeester, H.J.M. Interpretation of the Gerischer impedance in solid state ionics. *Solid State Ion.* **2003**, *157*, 29–33. [CrossRef]
63. Ascolani-Yael, J.; Montenegro-Hernández, A.; Garcés, D.; Liu, Q.; Wang, H.; Yakal-Kremski, K.; Barnett, S.; Mogni, J. The oxygen reduction reaction in solid oxide fuel cells: From kinetic parameters measurements to electrode design. *J. Phys. Energy* **2020**, *2*, 042004. [CrossRef]
64. Adler, S.B.; Lane, J.A.; Steele, B.C.H. Electrode kinetics of porous mixed-conducting oxygen electrodes. *J. Electrochem. Soc.* **1996**, *143*, 3554–3564. [CrossRef]
65. Pikalova, E.Y.; Bogdanovich, N.M.; Kolchugin, A.A.; Osinkin, D.A.; Bronin, D.I. Electrical and electrochemical properties of $La_2NiO_{4+\delta}$-based cathodes in contact with $Ce_{0.8}Sm_{0.2}O_{2-\delta}$ electrolyte. *Procedia Eng.* **2014**, *98*, 105–110. [CrossRef]
66. Lu, Y.; Kreller, C.; Adler, S.B. Measurement and modeling of the impedance characteristics of porous $La_{1-x}Sr_xCoO_{3-\delta}$ electrodes. *J. Electrochem. Soc.* **2009**, *156*, B513–B525. [CrossRef]
67. Adler, S.B. Factors governing oxygen reduction in solid oxide fuel cell cathodes. *Chem. Rev.* **2004**, *104*, 4791–4844. [CrossRef]
68. Yu, H.-C.; Adler, S.B.; Barnett, S.A.; Thornton, K. Simulation of the diffusional impedance and application to the characterization of electrodes with complex microstructures. *Electrochim. Acta* **2020**, *354*, 136534. [CrossRef]
69. Sadykov, V.A.; Sadovskaya, E.M.; Eremeev, N.F.; Pikalova, E.Y.; Bogdanovich, N.M.; Filonova, E.A.; Krieger, T.A.; Fedorova, Y.E.; Krasnov, A.V.; Skriabin, P.I.; et al. Novel materials for solid oxide fuel cells cathodes and oxygen separation membranes: Fundamentals of oxygen transport and performance. *Carbon Resour. Convers.* **2020**, *3*, 112–121. [CrossRef]
70. Gilev, A.R.; Kiselev, E.A.; Cherepanov, V.A. Performance of the lanthanum gallate based solid oxide fuel cells with the $La_{2-x}Ca_xNi_{1-y}Fe_yO_{4+\delta}$ cathodes and $Sr_2Ni_{0.75}Mg_{0.25}MoO_{6-\delta}$ anode. *Solid State Ion.* **2019**, *339*, 115001. [CrossRef]
71. Ananyev, M.V.; Kurumchin, E.K.; Porotnikova, N.M. Effect of oxygen nonstoichiometry on kinetics of oxygen exchange and diffusion in lanthanum-strontium cobaltites. *Russ. J. Electrochem.* **2010**, *46*, 789–797. [CrossRef]
72. Sadykov, V.A.; Eremeev, N.F.; Bolotov, V.A.; Tanashev, Y.Y.; Fedorova, Y.E.; Amanbayeva, D.G.; Bobin, A.S.; Sadovskaya, E.M.; Muzykantov, V.S.; Pelipenko, V.V.; et al. The effect of microwave sintering on stability and oxygen mobility of praseodymium nickelates-cobaltites and their nanocomposites. *Solid State Ion.* **2016**, *288*, 76–81. [CrossRef]
73. Boreskov, G.K.; Kasatkina, L.A.; Amerikov, V.G. Homomolecular isotope exchange of CO_2 on IV period metal oxides. *Kinet. Catal.* **1969**, *10*, 102–112.
74. Adler, S.B.; Chen, X.Y.; Wilson, J.R. Mechanisms and rate laws for oxygen exchange on mixed-conducting oxide surfaces. *J. Catal.* **2007**, *245*, 91–109. [CrossRef]
75. Amerikov, V.G.; Kasatkina, L.A.; Popova, G.Y. Study of CO_2 isotope exchange kinetics on the surface of chromium oxide. *Kinet. Catal.* **1968**, *9*, 429–432.
76. Kumar Gunda, N.S.; Choi, H.-W.; Berson, A.; Kenney, B.; Karan, K.; Pharoah, J.G.; Mitra, S.K. Focused ion beam-scanning electron microscopy on solid-oxide fuel-cell electrode: Image analysis and computing effective transport properties. *J. Power Source* **2011**, *196*, 3592–3603. [CrossRef]
77. Ananyev, M.V.; Farlenkov, A.S.; Eremin, V.A.; Kurumchin, E.K. Degradation kinetics of LSM-YSZ cathode materials for SOFC. *Int. J. Hydrogen Energy* **2018**, *43*, 951–959. [CrossRef]